minerals

MDPI

Article

Analysis of the Chemical and Radiological Risks Associated with Wastes from Mining in the Iberian Pyrite Belt

Juan Antonio Ramírez-Pérez [1], Manuel Jesús Gázquez-González [2], Felipe Jesús González-Barrionuevo [3] and Juan Pedro Bolívar [1,*]

[1] Department of Integrated Sciences, Center for Natural Resources, Health and Environment (RENSMA), University of Huelva, 21071 Huelva, Spain; juan.ramirez@dci.uhu.es
[2] Department of Applied Physics, Instituto de Investigación Marina (INMAR), University of Cádiz, 11510 Puerto Real, Spain; manueljesus.gazquez@uca.es
[3] Department of Earth Sciences, University of Huelva, 21071 Huelva, Spain; fbarrio@uhu.es
* Correspondence: bolivar@uhu.es

Abstract

Mining activities in the Iberian Pyrite Belt have generated large volumes of legacy wastes that may pose both environmental and radiological concerns, potentially limiting their reuse and valorization. However, integrated assessments combining chemical, mineralogical, and radiological characterization of these materials remain scarce. In this work, representative mining wastes from twelve sites across the Iberian Pyrite Belt were investigated through X-ray fluorescence, X-ray diffraction, scanning electron microscopy, standardized leaching tests, alpha and gamma spectrometry, and radon emanation measurements. The results revealed significant enrichment in potentially toxic elements, particularly Cu, Zn, Pb, and As, with concentrations exceeding local soil background values by up to several orders of magnitude. Leaching tests identified oxidized sulfide-rich residues as the materials with the highest pollutant mobility and greatest acid-generating potential. In contrast, radiological characterization showed that uranium-series, thorium-series radionuclides, and ^{40}K activities, together with radiological hazard indices and radon exhalation rates, were generally comparable to those of surrounding natural soils and remained below internationally recommended limits. These findings indicate that chemical contamination represents the main environmental constraint of these wastes, whereas radiological impact is generally low, supporting their case-by-case evaluation for remediation, valorization, and potential exclusion from radiological control.

Keywords: Iberian Pyrite Belt; mining wastes; acid mine drainage; NORM; radionuclides; leaching behavior; radiological hazard; radon exhalation; waste valorization

Academic Editor: Robert Šajn

Received: 26 May 2026
Revised: 12 June 2026
Accepted: 16 June 2026
Published: 18 June 2026

1. Introduction

Mining activities have generated large volumes of wastes worldwide, many of which remain stored in abandoned deposits, ponds, heaps, and tailings facilities [1]. These materials often contain elevated concentrations of potentially toxic elements, sulfide minerals, and residual valuable metals, making them both an environmental liability and a potential secondary resource within circular economy strategies [2,3]. Their long-term exposure to atmospheric conditions can promote oxidation, acid generation, metal mobilization, dust dispersion, and contamination of surrounding soils and waters, especially in historical mining districts [4]. In parallel, some mining residues may also contain enhanced concentrations of naturally occurring radionuclides, leading to their classification as Naturally

Occurring Radioactive Material (NORM) and requiring radiological evaluation before reuse or disposal [5,6].

The Iberian Pyrite Belt (IPB), extending across southwestern Spain and southern Portugal, is one of the largest volcanogenic massive sulfide provinces in the world and has been exploited for thousands of years [7]. Its ores, dominated by pyrite (FeS_2) with variable contents of Cu, Zn, Pb, Ag and other metals, supported intense mining and metallurgical activity, particularly during the nineteenth and twentieth centuries [8]. As a consequence, numerous legacy waste deposits (legacy sites) remain distributed throughout the region [9].

Previous studies in the IPB have mainly focused on acid mine drainage generation, metal dispersion, environmental contamination, and recovery of strategic elements from wastes [10–12]. These investigations have shown that many residues contain significant concentrations of metals/metalloids (As, Cu, Pb, Zn, Cd) and other hazardous elements, with substantial leaching potential under acidic conditions [13]. At the same time, some wastes still retain economic interest due to residual metal grades or useful mineral phases, supporting the idea of mine waste revalorization [14]. However, a major challenge lies in balancing resource recovery with environmental safety, since remediation-oriented approaches may conflict with exploitation-based strategies.

Compared with their chemical characterization, the radiological behavior of IPB wastes has received considerably less attention. Sulfide mining and associated metallurgical industries are commonly considered NORM activities because uranium- and thorium-series radionuclides can be redistributed during roasting, smelting, hydrometallurgical extraction, or waste concentration processes [15,16]. Although some studies have reported moderate external gamma hazards, important uncertainties remain regarding variability among residue types, radionuclide partitioning, and radon release potential, particularly for fine-grained materials that could be reused in civil applications [17]. This aspect is especially relevant because European regulations increasingly require radiological screening of industrial byproducts and construction materials [18].

Therefore, a comprehensive and integrated assessment of mining residues from the IPB is still needed. Most published works address either geochemical contamination, mineral processing potential, or radiological aspects separately, whereas combined chemical–mineralogical–radiological evaluations remain scarce [19]. Such integrated studies are essential to determine whether these materials should be managed as hazardous wastes, reprocessed as secondary resources, reused in engineering applications, or reclassified under NORM criteria.

In this context, the present work investigates a wide range of representative mining wastes from the Iberian Pyrite Belt through multi-element chemical analysis, mineralogical and morphological characterization, leaching tests, and radiological assessment. Natural radionuclides were determined together with radiological hazard indices, radon emanation factors, and exhalation rates. The results confirm that several residues exhibit high environmental risk due to toxic element mobility, whereas their radiological impact is generally comparable to that of natural soils from the surrounding area and strongly dependent on residue type. This suggests that some materials could potentially be excluded from NORM classification or considered for regulatory declassification. Overall, these findings provide a scientific basis for prioritizing remediation measures, identifying valorization opportunities, and evaluating the suitability of these wastes for reuse.

2. Materials and Methods

2.1. Study Area, Samplings and Pre-Treatment

For this work, twelve mining districts from the Iberian Pyrite Belt were selected based on the nature of the wastes present, their historical production records, and their

environmental relevance. The selected areas were Tharsis (TH), Lagunazo (LA), Cueva de la Mora (CM), San Telmo (ST), Zarza-Perrunal (ZP), Riotinto (RT), the Almagrera ponds at Sotiel Coronada (SC), Cabezas del Pasto (CP), Nuestra Señora del Carmen (CA), São Domingos (SD), Herrerías (HE), and Cobre las Cruces (CC). Their geographical distribution is shown in Figure 1. With the exception of Cobre las Cruces, situated in the province of Seville, and São Domingos, located in the Portuguese Alentejo region, all remaining sites are within Huelva province.

Figure 1. Geographical distribution of the studied mining sites. Coordinates are provided in the ETRS89/UTM 29N reference system. Base image obtained from Google Earth. Site codes: Tharsis (TH), Lagunazo (LA), Cueva de la Mora (CM), San Telmo (ST), Zarza-Perrunal (ZP), Riotinto (RT), Sotiel Coronada (SC), Cabezas del Pasto (CP), Nuestra Señora del Carmen (CA), São Domingos (SD), Herrerías (HE), and Cobre las Cruces (CC).

Field campaigns were carried out from April 2023 to March 2025. In order to reduce the effects of surface weathering, the top 5 cm layer was first removed prior to sampling. At each site, the collected material corresponded to a composite sample obtained from several subsampling points within the waste deposit in order to reduce the effect of local heterogeneity and improve representativeness. Samples were collected with a shovel and preserved for later pre-treatment procedures, including drying and grinding. This amount was considered adequate to ensure enough material for both multi-elemental and radiological analyses, while still allowing practical handling and transport.

Several types of mining wastes were investigated in this study. Roasted pyrite corresponds to the reddish residue left after sulfur removal from polymetallic sulfides during roasting processes [20]. Slags are solid byproducts formed during the smelting of sulfide ores at temperatures close to 1200 °C and subsequently cooled after recovery of target metals [21]. Jarosite pond materials are mainly composed of the yellow iron hydroxy sulfate mineral $KFe_3(SO_4)_2(OH)_6$ which precipitates in strongly acidic waters (pH < 3) enriched in Fe^{3+} and sulfate, conditions commonly linked to acid mine drainage and usually accumulates in low flow or stagnant areas [22]. In addition, flotation tailings of pyrite were considered; these are wastes produced during the concentration of valuable minerals by froth flotation using injected air bubbles [23]. Cementation wastes are residues generated during the recovery of copper from acidic leachates produced in mining and hydrometallurgical processes. In cementation channels filled with iron scrap, dissolved Cu^{2+} is reduced by metallic iron, precipitating elemental copper (“cement copper”) and iron oxyhydroxides [24].

Other waste studied was leached pyrite, produced during the processing of pyrite ores with sulfuric acid, typically obtained from roasting operations, in order to recover economically valuable metals such as Cu or Pb [25]. Additional materials were also analyzed, including atmospheric pressure leach residues from the active Cobre las Cruces hydrometallurgical plant, rejected shales from overburden removal, and degraded mine structures/buildings potentially affected by contaminated leachates. Secondary pond wastes from the Lagunazo mine, formed by precipitation of metal-rich phases in accumulated waters, were likewise considered. Where required, uncontaminated background soils were also sampled at each mining site.

2.2. Multi-Elemental Composition

The elemental composition of the samples was determined by X-ray fluorescence (XRF), focusing on the quantification of major elements. Analyses were performed using a PANalytical ZETIUM sequential spectrometer (Almelo, The Netherlands) at the Centro de Investigación, Tecnología e Innovación (CITIUS), University of Seville (Spain). The instrument is equipped with a 4 kW X-ray tube with a Rh anode and front window, two detectors (flow and scintillation), and five analytical crystals (PX1, PE 002, LiF 200, Ge 111, and LiF 220). For each dried sample, an aliquot of 1.5 g was prepared. Quality control procedures included the use of blanks, replicates, and certified reference materials (CRMs).

2.3. Mineralogy

Mineralogical characterization was performed by X-ray diffraction (XRD). Prior to analysis, samples were mixed with 12% zincite (ZnO) as an internal standard to enable the determination of the amorphous fraction through Rietveld refinement. After homogenization, the prepared samples were sent to the CITIUS for analysis.

Measurements were carried out using a Bruker D8 ADVANCE A25 (Karlsruhe, Germany) powder diffractometer operating in Bragg–Brentano geometry, equipped with a Cu X-ray tube, Soller slits, a motorized primary slit, a linear detector, and an optional sample rotation system. The instrument also features a 90-position programmable sample changer. Data acquisition was performed under the following conditions: 2θ range of 3–70°, step size of 0.015°, and counting time of 0.1 s per step, with tube settings of 40 kV and 30 mA. A fixed divergence slit of 0.5°, sample rotation at 30 rpm, and a nickel filter were employed.

The obtained diffraction patterns were subsequently analyzed both qualitatively and quantitatively using DIFFRAC.EVA version 7.0 and DIFFRAC.TOPAS version 5.0 software (Karlsruhe, Germany), applying Rietveld refinement in the latter [26]. Additionally, PROFEX version 5.6.0 software (Bettlach, Switzerland) was used for a preliminary identification of crystalline phases.

2.4. Microstructure

A semi-quantitative characterization of the waste, including chemical composition and microstructure, was performed by scanning electron microscopy coupled with energy-dispersive X-ray spectroscopy (SEM-EDS). This technique is based on the interaction between a focused electron beam and the sample surface, generating signals that provide information on morphology, composition, and crystal features. Analyses were carried out using a JEOL JSM-5410 microscope (Tokyo, Japan) at the University of Huelva (Spain).

Samples were prepared by embedding in epoxy resin (Araldite®, Basel, Switzerland), followed by grinding with silicon carbide (SiC) paper and polishing with diamond pastes of 6, 3, and 1 μm. The polished surfaces were then etched with 5% HF for 10 s to enhance phase identification. Afterwards, the samples were ultrasonically cleaned with distilled water and ethanol, dried under controlled conditions to avoid structural damage, and

coated with a thin Au–Pd layer using a sputter coater to ensure electrical conductivity during SEM observation.

2.5. Leaching Test

Element mobility and potential environmental risk were assessed through a leaching test conducted according to the UNE-EN 12457-4 standard ("Characterization of waste—Leaching—Compliance test for leaching of granular waste materials and sludges—Part 4: One-stage batch test at a liquid-to-solid ratio of 10 L kg^{-1} for materials with particle size below 10 mm" [27]). This procedure evaluates the release of soluble components under water contact, considered the main mechanism driving contaminant mobilization during waste reuse or disposal.

The method is specifically designed for granular materials and sludges with particle sizes under 10 mm and focuses on the behavior of inorganic constituents. After 24 h of agitation, the suspensions were filtered through a 0.45 µm membrane. The resulting leachates were analyzed by inductively coupled plasma mass spectrometry (ICP-MS) and inductively coupled plasma optical emission spectrometry (ICP-OES).

Additionally, the transfer factor (TF) for each element in the leachate was calculated. This parameter represents the ratio between the amount of a given element released into the aqueous phase and its total content in the solid material. The TF was determined using the following expression:

$$TF\ (\%) = 100 \cdot C_{lix} / C_{sow}, \quad (1)$$

where C_{lix} corresponds to the concentration of element "x" in the leachate, and C_{sow} represents its concentration in the original solid waste. Both values are expressed in µg g^{-1} relative to the initial material.

2.6. Radioactive Characterization

Radioactive characterization was performed using two complementary low-level radiometric techniques: alpha-particle spectrometry and gamma spectrometry.

For alpha spectrometry, a sequential radiochemical procedure was applied to isolate actinides (mainly uranium and thorium isotopes) together with ^{210}Po. Initially, tracers ^{229}Th, ^{232}U and ^{209}Po were added to determine chemical recoveries. Approximately 0.5 g of sample was subsequently digested in closed vessels using a mixture of concentrated acids (3 mL of 65% HNO_3, 1 mL of 37% HCl, and 8 mL of 40% HF). Separation of Po, U, and Th was then carried out using the tributyl phosphate (TBP) extraction method [28]. Finally, uranium and thorium were electrodeposited onto suitable supports, while polonium was deposited by spontaneous plating [29]. Measurements were conducted using PIPS-type ion-implanted silicon detectors (EG&G Ortec), and spectra were processed with Genie 2000 software. The alpha emitting radionuclides determined included ^{238}U, ^{235}U, ^{234}U, ^{232}Th, ^{230}Th and ^{210}Po.

Gamma spectrometry was employed to determine the activity concentrations of gamma-emitting radionuclides. Measurements were carried out using a high-purity germanium (HPGe) detector with extended range (XtRa) and a thin beryllium window, allowing detection of low-energy emissions down to approximately 20 keV. The system was equipped with a nitrogen-purged shielding to reduce background radiation by eliminating radon. The detector exhibited an efficiency of 38.4% at 1332 keV (relative to a 3″ × 3″ NaI(Tl) detector), a full width at half maximum (FWHM) of 1.74 keV at 1332 keV and 0.88 keV at 122 keV, and a Compton-to-peak ratio of 67.5:1 [30,31]. The radionuclides analyzed included ^{234}Th (63.29 keV), ^{226}Ra (186.2 keV), ^{210}Pb (46.52 keV), and ^{40}K (1460.83 keV). In addition, ^{228}Ra and ^{228}Th were indirectly assessed through their secular equilibrium with ^{228}Ac (911 keV) and ^{212}Pb (238 keV), respectively [32].

Quality assurance for both techniques included the analysis of procedural blanks (one per ten samples), replicates, and certified reference materials (IAEA-434, IAEA-375, and IAEA-327), as well as participation in intercomparison exercises to ensure accuracy and reproducibility.

2.7. Radiological Hazard Indexes

An important parameter for evaluating radiological risk is the radium equivalent activity (Ra_{eq}). This index combines the activity concentrations of ^{238}U, ^{232}Th and ^{40}K into a single representative value, considering the external gamma radiation hazards associated with these radionuclides and their decay products under secular equilibrium conditions. Raeq expresses the total radioactivity as an equivalent concentration that would produce the same external dose rate, according to the following equation [33,34]:

$$Ra_{eq}\ (Bq\ kg^{-1}) = C_U + 1.43C_{Th} + 0.077C_K, \quad (2)$$

where C_U, C_{Th} and C_K correspond to the activity concentrations of ^{238}U, ^{232}Th and ^{40}K, respectively, expressed in Bq kg^{-1}. According to the United States Environmental Protection Agency (USEPA), materials with Raeq values below 370 Bq kg^{-1} are generally regarded as safe for unrestricted use [35].

The external hazard index (H_{ex}) is another widely used indicator, employed to estimate the gamma radiation dose arising from naturally occurring radionuclides in construction materials, especially in confined environments such as dwellings or wells. It can be determined using the following equation [36,37]:

$$H_{ex} = C_U/370 + C_{Th}/259 + C_K/4810. \quad (3)$$

The annual effective dose is expected to remain below 1 mSv y^{-1} when H_{ex} is less than 1 [35]. In addition, the European Union guideline Radiation Protection 112 established the activity concentration index (I_c) as a criterion for evaluating gamma radiation from building materials. This parameter is calculated using the following expression [5]:

$$I_c = C_{Ra}/300 + C_{Th}/200 + C_K/3000, \quad (4)$$

where C_{Ra} denotes the activity concentration of ^{226}Ra, expressed in Bq kg^{-1}. For building materials (cement and concrete) containing naturally occurring radioactive constituents, such as fly ash, phosphogypsum, or slag, the recommended I_c value should not exceed 1. In the case of superficial or restricted-use materials, including tiles and boards, values up to 6 may be considered acceptable.

2.8. Radon Emanation and Exhalation

According to European Directive 2013/59/Euratom, indoor radon concentrations should not exceed 300 Bq m^{-3}. Therefore, if these mining residues are to be considered as potential construction materials, it is necessary to evaluate their radon emanation factor and exhalation rate [5]. Both parameters were determined by placing equally ground and homogenized residues inside a sealed accumulation chamber (polypropylene box). Once closed, the radon concentration inside was monitored and the accumulation curve was recorded (Figure 2), continuously extracting the internal air and returning it after passing through the radon monitor (RAD7 or ARAD RTM) in a closed-loop recirculation system [38]. The accumulation curve follows the expression [39]:

$$C(t) = C_{sat}(1 - e^{-t\lambda ef}), \quad (5)$$

where C_{sat} denotes the saturation concentration, while λ_{ef} represents the effective decay constant. This parameter results from the combination of the radon decay constant (λ_{Rn}), the leakage loss constant (λ_f), and the back diffusion constant (λ_b). By adjusting the experimental data to Equation (5), these parameters can be derived. Consequently, the emanation factor (ε) and the exhalation rate (E_0) were obtained using the following equations [39]:

$$\varepsilon = (\lambda_{ef}\, C_{sat}\, V)/(\lambda_{Rn}\, C_{ra}\, m), \quad (6)$$

$$E_0 = (\lambda_{ef}\, C_{sat}\, V)/(S), \quad (7)$$

where V is the accumulation volume (including the volume of the radon detector), S is the exhalation surface of the sample, m is the sample mass, and C_{ra} is the ^{226}Ra activity concentration of the tested material.

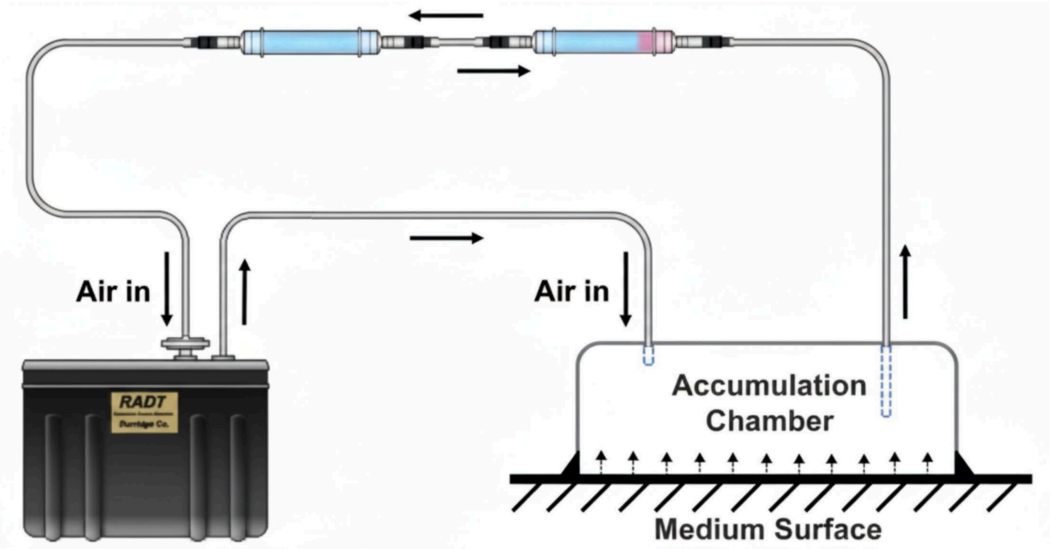

Figure 2. Schematic representation of the accumulation chamber with the sample placed inside, where air is continuously recirculated through the radon monitor.

3. Results and Discussions

3.1. Major Elements

The concentrations of major elements by XRF are presented in Figure 3, including the mean values for each waste type. The relatively low dispersion observed within each group indicates that each residue displays a characteristic geochemical signature controlled by its lithology, metallurgical treatment and post-depositional weathering.

Pyrite flotation residues (FPY) are distinguished by their extremely high sulfur content (42.5% on average), exceeding typical IPB soil values by several orders of magnitude [40]. Together with the elevated Fe concentration (15.9%) related to a typical soil [41], this confirms the presence of abundant residual pyrite that remained unprocessed after flotation. These wastes also contain some of the highest concentrations of Cu (0.4%) and Zn (1.3%) among all materials studied, indicating a substantial inventory of toxic contaminants. Their strong sulfur enrichment implies a high acid-generating potential and makes them one of the most relevant sources of acid mine drainage (AMD) [42].

Roasted pyrite ashes wastes (RPA) are dominated by Fe (50.2% on average), consistent with oxidation during roasting and the formation of iron oxide-rich ashes. Sulfur contents are lower than flotation residues due to thermal decomposition, although still above natural soil levels. Calcium (0.86%) is moderately enriched, whereas Al (0.67%) and K (0.16%) remain below background concentrations [41]. These residues also show elevated Cu (0.24%), Pb (1.1%), Zn (1.0%) and As (0.8%) contents, reflecting the incomplete volatilization or concentration of trace metals during roasting. Weathering of these ashes may mobilize toxic elements, particularly under acidic conditions.

Smelting slags (SLA) present a distinctive chemistry characterized by high Ca (1.20%), Fe (25.2%) and Si (16.0%), reflecting the use of fluxes and the metallurgical separation process [32]. They also contain comparatively high Al (3.4%), suggesting possible reuse potential as secondary raw material. Sulfur is lowest in this residue type (0.5%), indicating limited acid-generation capacity relative to sulfidic wastes. However, slags still retain anomalous concentrations of Pb (0.5%), Zn (1.3%), Cu (0.3%) and As (0.4%) trapped within glassy or crystalline phases, which may become available during long-term weathering.

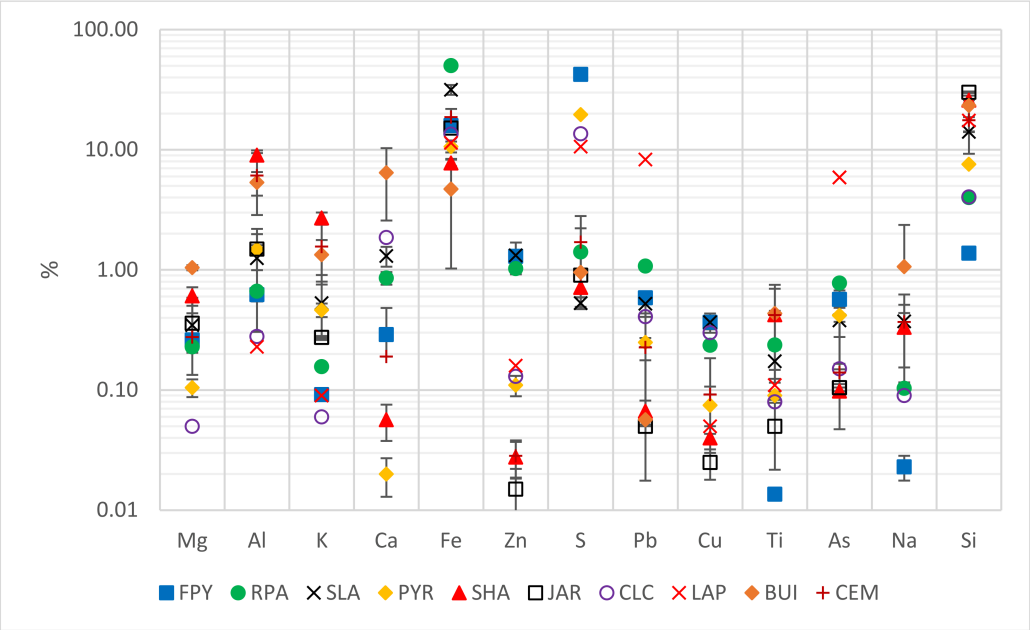

Figure 3. Mean values for major elements concentrations for floated pyrite (FPY), roasted pyrite ashes (RPA), slags (SLA), leached pyrite (PYR), shale rejects (SHA), jarosite pond (JAR), Cobre las Cruces waste (CLC), Lagunazo pond (LAP), abandoned buildings (BUI) and cementation (CEM). Standard deviations from the mean are included in the margins of error.

Leached pyrite residues (PYR) preserve the Fe–S signature of pyritic materials, with 10.6% Fe and 19.6% S. Minor elements such as Mg (0.11%), Al (1.5%), K (0.5%) and Ti (0.1%) occur near the lower range of IPB soils, whereas Ca is scarce (0.02%). Despite previous processing, these wastes still contain significant sulfur and residual metals, so they remain capable of generating acidic leachates and releasing contaminants.

Shale rejects (SHA) display a broadly consistent composition with typical shale materials, being dominated by Si (25.8%) and other elements such as Al (9.01%), K (2.7%), Mg (0.61%) and Ti (0.42%) among the studied wastes. This elemental association is characteristic of quartz and phyllosilicate-rich lithologies, confirming their derivation from country-rock materials [43].

Jarosite ($KFe_3(SO_4)_2(OH)_6$) pond (JAR) waste is mainly composed of Fe (15%) and Si (30%), with lower concentrations of Al (1.49%), Mg (0.36%), K (0.28%) and S (0.9%). As these values differ from the theoretical composition of pure jarosite, the residue likely

contains significant amounts of quartz, silicates and poorly crystalline Fe phases in addition to jarosite-group minerals, consistent with previous observations in the Riotinto area [44]. Minor Zn, Pb, Cu and As contents also indicate trace metal contamination above typical soil levels [45].

The bulk composition of Cobre las Cruces (CLC) is dominated by sulfur and iron with a 13.6% and 13.5% respectively. Other minor elements that compose this waste are silica (4.1%) and calcium (1.9%). These results suggest the material is strongly rich in minerals such as pyrite, gypsum and minor silicates. Minor Pb (0.41%), As (0.15%), Cu (0.30%) and Zn (0.13%) indicate trace metal enrichment typical of oxidized massive sulfide wastes and warrant attention because such trace elements can become mobile under acidic or saline conditions [46].

Building material waste (BUI) is dominated by Si (23.45%), Ca (6.44%) and Al (5.34%), consistent with mortars, concretes, bricks and other aluminosilicate construction products [47]. Moderate Fe contents (4.71%) may reflect aggregates, weathering inputs or corrosion residues, while measurable S (0.95%) suggests secondary sulfate formation after interaction with acid mine drainage. Trace Pb (0.06%) also indicates contamination from nearby legacy sulfide wastes.

Cementation waste (CEM) shows an Fe-rich composition (18.7%), consistent with iron oxyhydroxides precipitated during historical copper recovery from acidic mine waters. Significant Si (17.6%) and Al (6.1%) contents indicate contributions from aluminosilicate detritus, while K (1.6%) may derive from host rocks. Sulfur (1.7%) suggests residual sulfate phases formed under acidic conditions. Trace Pb, As and Cu contents indicate incomplete metal removal and their retention by adsorption or co-precipitation with Fe hydroxides [48].

The Lagunazo pond residue (LAP) shows a typical composition of AMD-related accumulation and precipitation processes, dominated by Fe (11.4%), Si (17.5%) and high S (10.6%), consistent with secondary iron sulfate phases such as schwertmannite or jarosite [49]. Exceptionally high As (5.90%) and Pb (8.30%) contents indicate strong scavenging and co-precipitation of toxic elements by Fe precipitates. Therefore, Lagunazo pond likely acts as a natural settling basin receiving AMD-derived leachates from nearby pyrite ash and slag wastes.

In general, Cu, Pb, Zn and As concentrations in all residues exceed typical soil values by one to four orders of magnitude, confirming widespread metal(loid) enrichment across the mining district [45]. Sulfur contents are also consistently above natural background levels, indicating a generalized capacity for acidity generation and AMD production. Previous studies in the IPB have also shown enhanced atmospheric dispersion of particulate pollutants such as Zn, Cu, As, Pb, Fe and S near waste deposits, as well as airborne As concentrations exceeding regulatory thresholds in some localities [50]. Therefore, these mining wastes represent not only geochemical archives of historical ore processing, but also persistent sources of environmental contamination with potential implications for soils, waters, air quality and human health [51].

3.2. Mineralogy

This section examines the different mineralogical phases identified by XRD in the most relevant mining wastes, including both crystalline minerals and the amorphous fraction. Their relative abundances are shown in Figure 4. The mining wastes analyzed in this section are: floated pyrite, roasted pyrite, slags, shales, leached pyrite and cementation

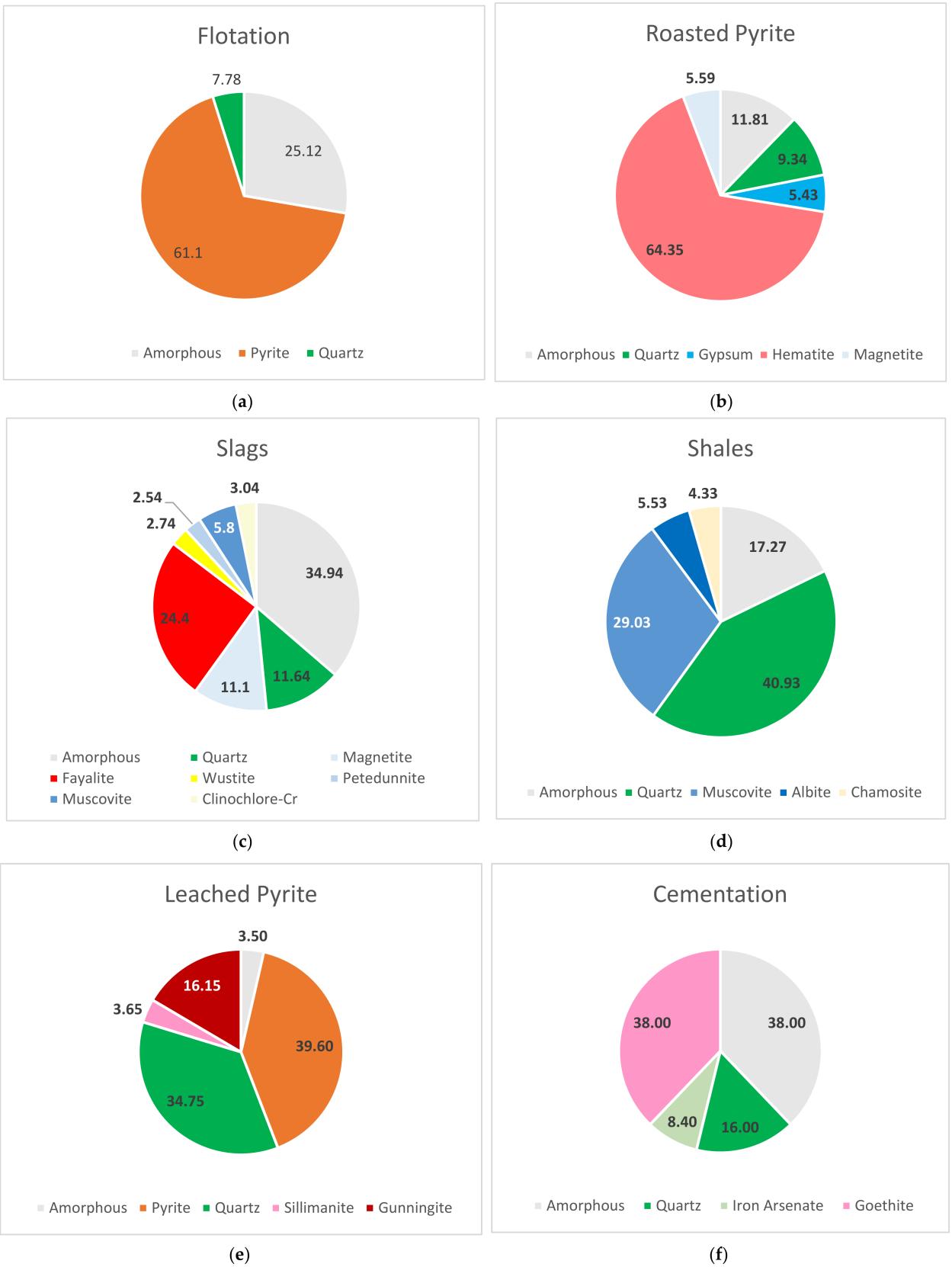

Figure 4. Average mineral concentrations in % of different mining wastes in the IPB: (**a**) floated pyrite; (**b**) roasted pyrite; (**c**) slags; (**d**) shales; (**e**) leached pyrite; (**f**) cementation.

First of all, pyrite flotation slags are mainly composed by pyrite (FeS_2, 61.1%), with minor quartz (SiO_2, 7.8%) and a substantial amorphous fraction (25.12%). The high pyrite

concentration in this residue is expectable because this mineral is not the main target during the flotation process. Furthermore, the dominance of pyrite is corroborated by the high S (42.5%) and Fe (15.9%) content previously studied by XRF, thus validating the results. Considering its origin, the amorphous phase may be iron hydroxides such as ferrihydrite ($Fe_5HO_8 \cdot H_2O$), due to its low structural order, generated by the partial oxidation of pyrite [52].

The mineralogical phases of pyrite roasting ash are characterized by high iron oxide content, such as hematite (Fe_2O_3) at 64.3% and magnetite (Fe_3O_4) at 5.6%. Also, there is a significant quartz (SiO_2) content with 9.3%. These results are also consistent with those previously obtained by XRF for Fe (~50%) and Si (2%–8%) concentrations.

The mineralogical composition of the smelting slags is consistent with materials derived from high-temperature pyrometallurgical processes applied to pyrite-rich ores. The notable abundance of fayalite (Fe_2SiO_4, 24.4%) is particularly diagnostic of iron silicate slags. This mineral is formed during smelting when iron oxides react with SiO_2 at temperatures above 1000 °C, indicating silica addition during the metallurgical operation [53]. This interpretation is consistent with XRF data, as slags contain around 20% of Si. The detection of magnetite (11.1%) reflects incomplete reduction conditions inside the furnace. Minor quartz (11.6%) and muscovite (5.8%) likely represent relict materials that did not fully melt during smelting process. The substantial amorphous fraction (~35%) is characteristic of rapidly cooled slags, where melt quenching prevents crystallization and leads to glassy matrixes dominated by Fe–Si–O compositions [54].

Shales exhibit a mineralogical assemblage dominated by quartz (~41%) and muscovite (~29%), with minor albite (5.5%) and chamosite (4.3%). This composition is typical of metasedimentary shales of the Iberian Pyrite Belt, where quartz-rich detrital material and phyllosilicates form the primary matrix, while albite reflects residual or slightly metamorphosed feldspar [55,56]. This mineralogy is consistent with XRF.

For leached pyrites, it can be seen that the content consists mainly of pyrite (39.6%) and quartz (34.8%). In addition, there is a significant amount of gunningite ($ZnSO_4 \cdot H_2O$, 16.2%) and, to a lesser extent, sillimanite (Al_2SiO_5, 3.7%). The high quartz content in the leached pyrite residues indicates that the pyrite deposits were not originally pure, but rather a mixture of both mineral phases, which were leached for the production of sulfuric acid. Similarly, XRF's results validate this mineralogy.

The mineralogical composition of the cementation wastes is dominated by goethite (FeO(OH), 38%) and large amorphous fraction (38%), accompanied by quartz (~16%) and a notable amount of iron arsenate (8.4%). This assemblage is characteristic of wastes generated during cementation processes in polymetallic mining districts such as the IPB, where dissolved Fe^{2+} and associated trace elements precipitate as Fe oxyhydroxides [57].

3.3. Morphology Characterization

FESEM technique provides valuable insight into the morphology of the samples, especially regarding their particle-size distribution, surface texture, and porosity. In this subsection, the mining wastes analyzed using this technique consisted of roasted pyrite ashes, flotation sludges, leached pyrites, slags and cementation, the most extended wastes along the IPB.

3.3.1. Roasted Pyrite

A representative FESEM image for roasted pyrite ashes is shown in Figure 5. Red area average yields 43.5% O, 37.0% Fe, 9.0% Si, 2.0% S, 1.6% Ca, 1.6% Zn and 1.5% Pb. This composition is fully consistent with the XRD mineralogy, which indicates a matrix dominated by iron oxides (hematite ~ 64%, magnetite ~ 5.6%), with subordinate quartz

(~ 9%), gypsum (~ 5.4%) and an ~11% amorphous fraction. The dominant signal of iron and oxygen reflects the hematite/magnetite matrix, the Si signal is attributable to quartz and/or amorphous silica, and the combined S and Ca signal is consistent with gypsum as a minor phase. Trace Zn and Pb are present at low but measurable levels. They are interpreted as being hosted in discrete secondary phases (zincite for Zn and anglesite for Pb). Also, these results are consistent with XRF analysis.

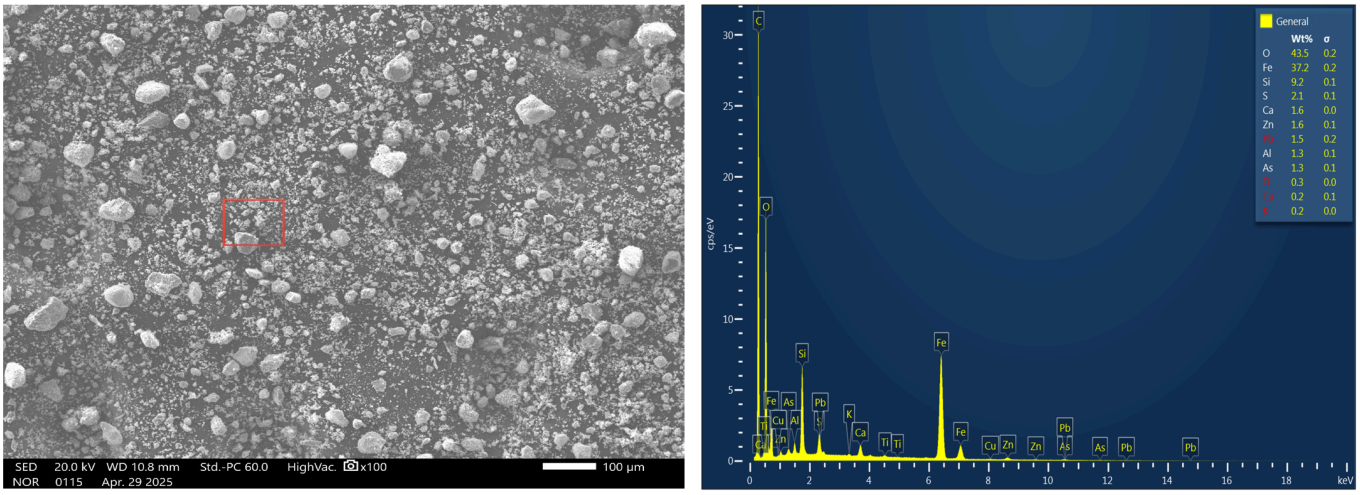

(**a**) (**b**)

Figure 5. FESEM analysis of roasted pyrite ashes. (**a**) Morphology of the sample. (**b**) General spectrum of the red box.

3.3.2. Floated Pyrite

A representative FESEM image for floated pyrite sludges is shown in Figure 6. Mean red square analysis shows 31.0% O, 28.6% Fe, 27.0% S, 3.7% Zn, 2.5% Si, and 2.5% Pb. This result reaffirms XRD analysis, being consistent with a matrix dominated with pyrite (61.1% by XRD), with minor contributions from amorphous material (~25%), quartz (~4.4%), and trace metal-rich secondary particles (Zn and Pb phases). The Fe and S signals reflect the bulk pyrite, while O originates from partial oxidation and amorphous oxides. Zn and Pb are present as discrete secondary particles, embedded in the pyrite matrix. Si corresponds to quartz and amorphous silicates. These results demonstrate the heterogeneous nature of the sludge and are consistent with the XRD-derived mineralogy, highlighting the predominance of pyrite and the low abundance of metal-bearing secondary phases. Also, XRF analysis is compatible with these results.

3.3.3. Slags

Slags FESEM image is shown in Figure 7. It can be observed that particles in the red box are mainly composed of 35.9% O, 34.9% Fe, 14.7% Si, 4.0% Ba, 3.7% Zn, 2.7% Ca, 1.7% S, and 1.6% Al. This heterogeneous composition, considering XRD analysis, is mainly composed by iron silicate phases (fayalite, Fe_2SiO_4) and iron oxides (magnetite, Fe_3O_4; wüstite, FeO), with minor quartz and muscovite. There is complete agreement between the results of both measurement techniques. Ba and Zn are present as minor metal-bearing phases, likely incorporated into the amorphous silicate fraction or present as discrete oxide/sulfate particles. Ca presence is justified by the phase obtained from smelting process, being part of a calcium silicate [21]. Al originates from muscovite or minor aluminosilicate inclusions.

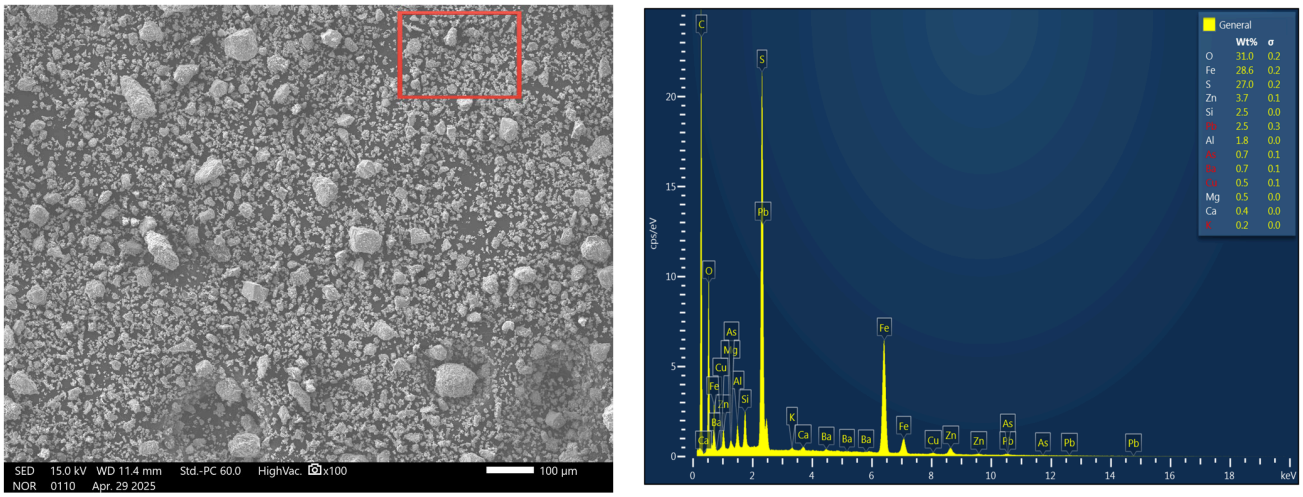

(**a**) (**b**)

Figure 6. FESEM analysis of floated pyrite sludge. (**a**) Morphology of the sample. (**b**) General spectrum of the red box.

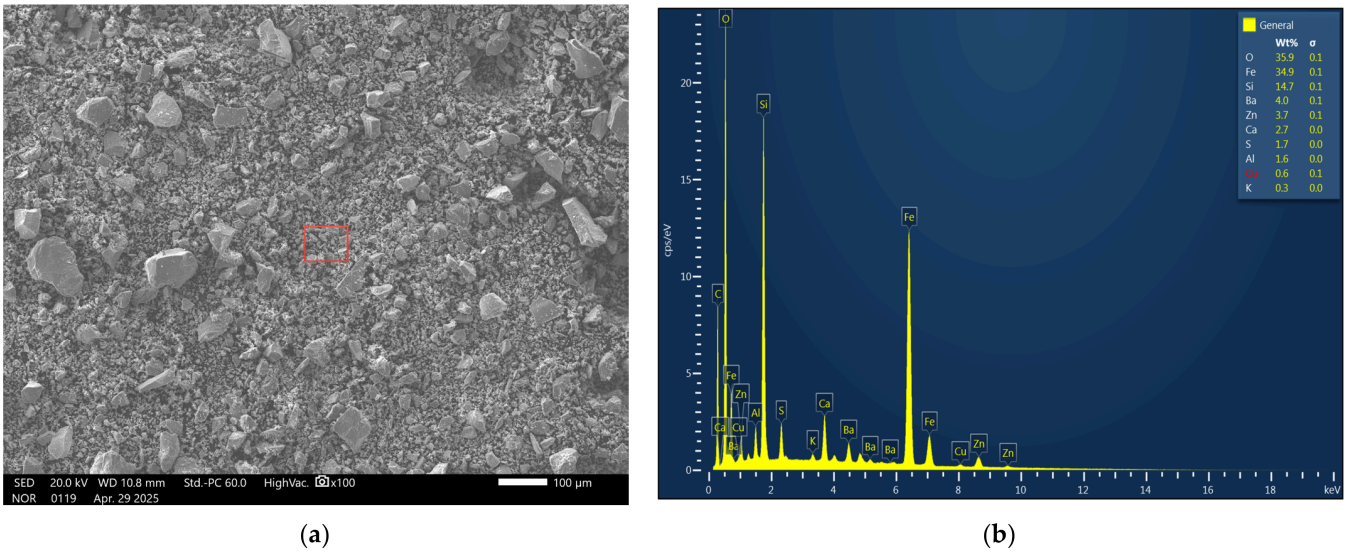

(**a**) (**b**)

Figure 7. FESEM analysis of slags. (**a**) Morphology of the sample. (**b**) General spectrum of the red box.

3.3.4. Leached Pyrites

A representative FESEM image for leached pyrites is shown in Figure 8. The average composition of analyzed global zone (red square; 36% O, 25% S, 24% Fe, 9% Si, 2.6% Al, 1.5% As and 1.2% K) is broadly consistent with the XRD-derived mineralogy, which indicates a pyrite-dominated assemblage with significant quartz and gunningite. Quantitative discrepancies, specifically the higher O, Fe and S and the lower Si detected, are attributed to the presence of fine-grained or amorphous secondary phases (oxides and sulfates) that contribute minimally to the crystalline XRD signal, and to sampling heterogeneity inherent to leached and oxidized residues. These observations suggest that surface oxidation products play a significant role in the elemental budget of the analyzed area

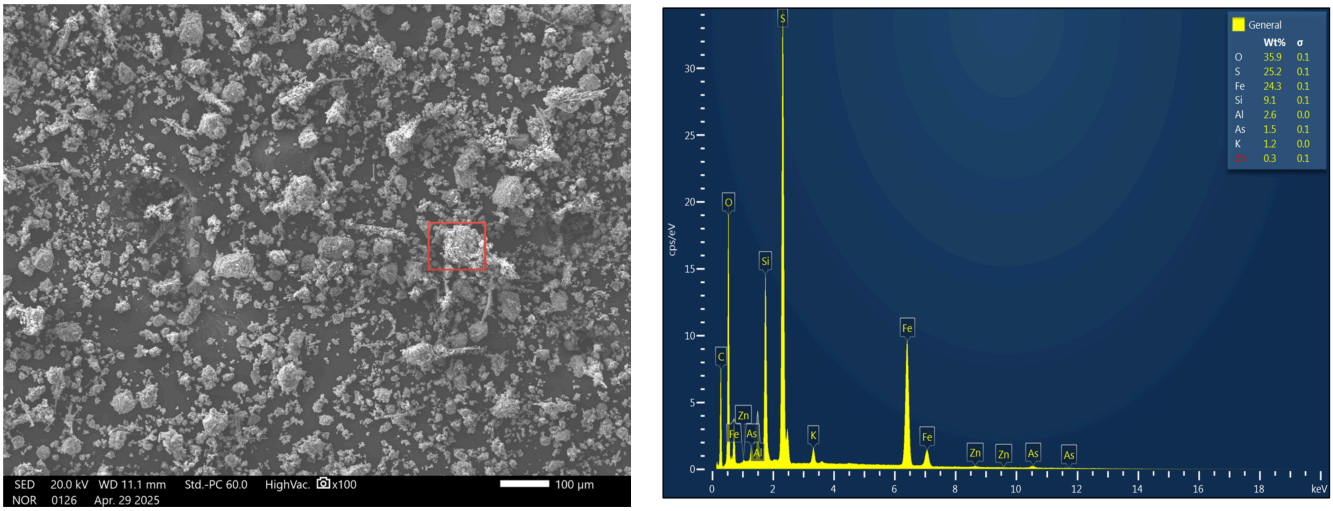

(**a**) (**b**)

Figure 8. FESEM analysis of leached pyrite. (**a**) Morphology of the sample. (**b**) General spectrum of the red box.

3.3.5. Cementation

FESEM image for cementation waste is shown on Figure 9. General spectrum of this waste yields 44.2% Fe, 40.8% O, 8.4% Si, 2.4% S, 1.9% Al and 0.8% As. These proportions are consistent with sampling a siliceous substrate (quartz) intimately associated with or coated by iron oxyhydroxide (goethite), in agreement with the bulk mineralogy (goethite 38%, quartz 16%, amorphous 38%). The substantial Al point local contributions from amorphous aluminosilicate materials. The low As concentration indicates that iron arsenate phases are spatially heterogeneous in the residue and that arsenic at this location is most likely present as a minor adsorbed or occluded component within the goethite/amorphous matrix rather than as a discrete arsenate crystal.

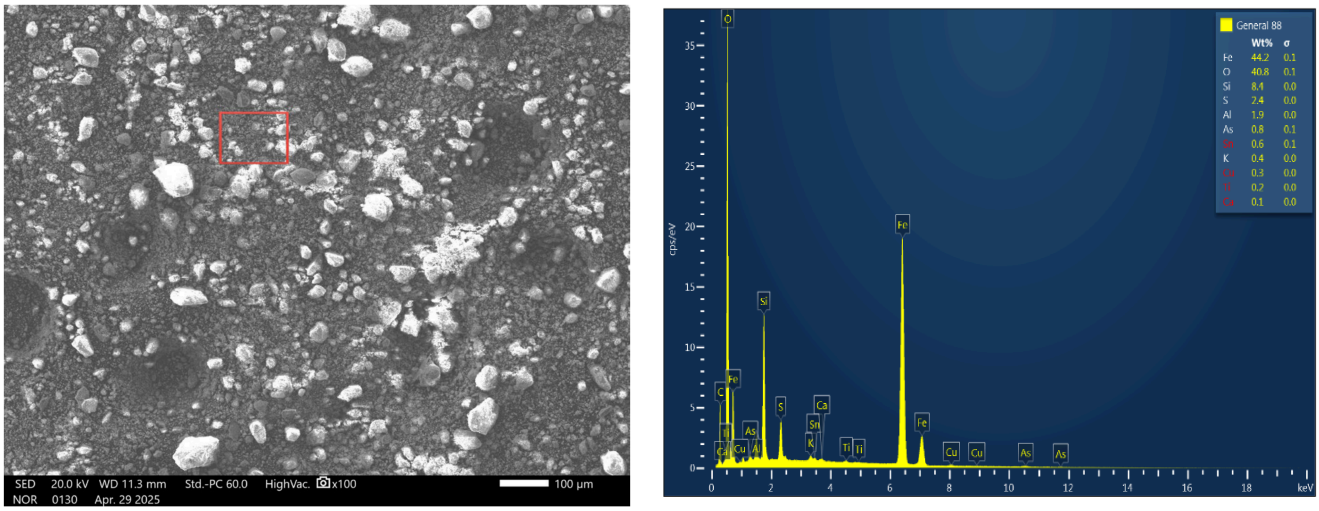

(**a**) (**b**)

Figure 9. FESEM analysis of cementation. (**a**) Morphology of the sample. (**b**) General spectrum of the red box.

3.4. Pollutant Mobility Assessed by Forced Leaching Tests

The objective of this test is to characterize the composition of the leachate generated under controlled conditions, thereby providing quantitative information on the aqueous

extraction of inorganic components from granular wastes and sludges. The concentration of the different elements in the leachates of the main mining wastes is shown in Figure 10. For this section, the most representative wastes that are distributed most widely throughout the entire IPB have been considered: floated pyrite, roasted pyrite, slags, leached pyrite, rejected shales and cementation wastes. Also, soils from IPB have been analyzed.

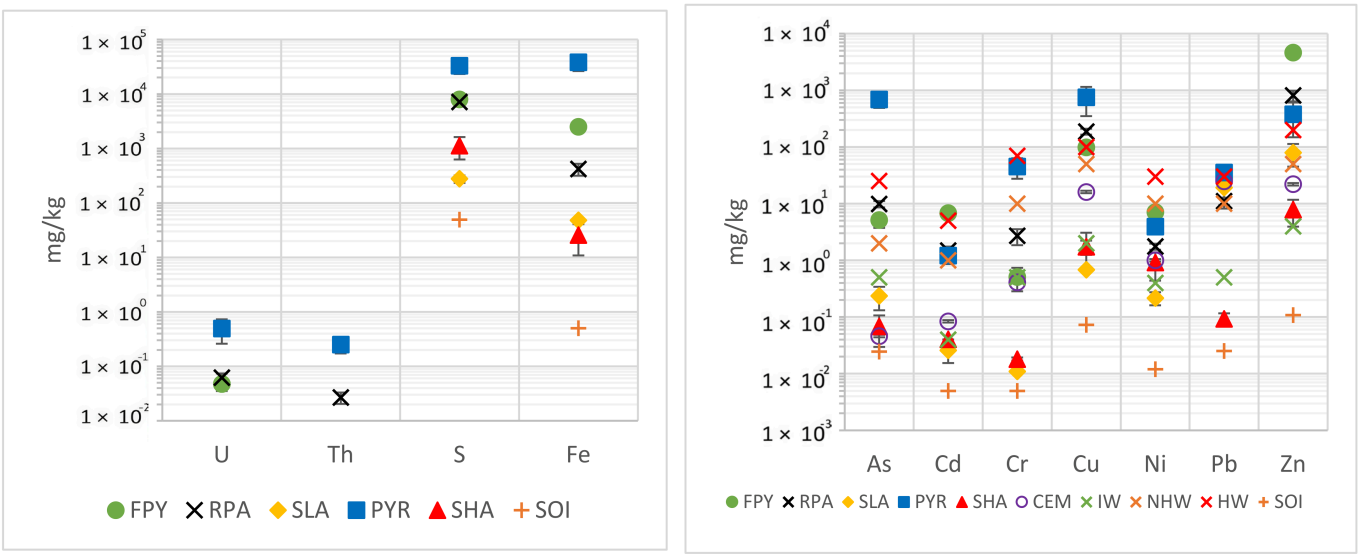

(**a**) (**b**)

Figure 10. (**a**) Elements' leached concentrations for U, Th, Fe, S. (**b**) Toxic metals/metalloids' leached concentrations. The classification values according to Decision 2003/33/EC for inert waste (IW), non-hazardous waste (NHW), and hazardous waste (HW) [58] and soil are also included.

The concentrations of U and Th measured in the leachates (Figure 10a) range between 10^{-2} and 100 mg kg^{-1} across all the analyzed waste materials. The behavior observed for Th is consistent with its well-known low geochemical mobility in iron-sulfide-rich systems, where this radionuclide tends to remain associated with solid phases [59]. In contrast, uranium generally exhibits higher mobility than thorium under oxidizing conditions, mainly due to the greater solubility of U species [60]. In the case of the leached pyrite wastes, the comparatively higher concentrations of U and Th relative to the other materials may be linked to the prior oxidation of pyrite. This process can promote the partial release of trace elements initially incorporated within the crystal lattice or retained in structural defects of the sulfide matrix [61]. It is noteworthy, however, that the concentrations of U and Th in all analyzed wastes remain below the threshold values recommended by the IAEA (3 mg kg^{-1}; ref. [62]). For the IPB soil samples (SOI), both U and Th concentrations are below the detection limit (0.005 mg kg−1), a situation similarly observed in the shale and slag samples. Finally, according to Li and colleagues for Canadian tailings, the concentrations of U and Th in the IPB waste leachates are of the same order of magnitude, except for the PYR sample, where uranium and thorium levels are approximately one order of magnitude higher [63].

The release of Fe is closely linked to the generation of acidity and the dissolution of secondary phases. In slags, cementation or shales, insoluble solid phases are formed, not exceeding the limits for iron in water according to European Union Water Framework Directive, 200 mg kg^{-1} [64]. For floated pyrite (2500 mg kg^{-1}) and leached pyrite (38,000 mg kg^{-1}), these concentrations are consequence of the high solubility of Fe in acidic conditions, typical of sulfide oxidation in IPB. Precisely, leached pyrite, the residue with the highest concentration of Fe in the leachate, has the lowest pH of those analyzed (pH = 2.24)

Sulfur is present in high concentrations in the leachates, especially in PYR and FPY, reaching values of around 104 mg kg^{-1}. This behavior is characteristic of sulfide-rich waste undergoing oxidation processes, where pyrite (FeS_2) is transformed into soluble sulfates, significantly increasing the S load in solution. Slags show the lowest concentrations of S (275 mg kg^{-1}), consistent with the prior removal of sulfates during hydrometallurgical processes and partial neutralization of the medium.

Figure 10b shows the leached concentrations for heavy metals and As from the different mining wastes, together with the landfill admission thresholds for inert (IW), non-hazardous (NHW), and hazardous waste (HW) established in Decision 2003/33/EC [58]. Overall, PYR and FPY exhibit the highest metal and metalloid release, frequently reaching or exceeding the HW limits, whereas SLA and CEM generally show lower concentrations, mostly within the IW–NHW ranges.

As, Cu, Pb and Zn are the most critical elements. Cu and Zn systematically exceed the HW thresholds in PYR, RPA and FPY between 1 and 20 times, reflecting the high mobility of these elements during sulfide oxidation processes typical of the Iberian Pyrite Belt [65]. Pb also shows elevated concentrations in PYR (35 mg kg^{-1}) surpassing the HW limit, likely due to the presence of relatively soluble secondary Pb-bearing phases under acidic conditions. In contrast, Cr and Ni remain below their respective HW limits in all samples, indicating limited mobility and strong association with low-solubility mineral phases. Cadmium shows low concentrations overall, although values close to the HW limit are observed in some PYR and FPY samples, consistent with their known mobility in acidic environments [66].

Furthermore, all analyzed waste materials generate leachates with metals/metalloids concentrations at least one order of magnitude higher than those released by uncontaminated soil (SOI). In particular, waste such as PYR or FPY can release concentrations up to five orders of magnitude higher. Also, when compared with other studies based on standardized leaching tests in mining environments, the concentrations obtained for most metals and metalloids are broadly consistent with previously reported values. Specifically, leachate concentrations from the analyzed mining wastes are comparable or one order of magnitude lower than those reported by Wang et al. [67]. However, the leached pyrite waste (PYR) stands out, as its metal and metalloid concentrations generally exceed those reported in the literature by approximately one order of magnitude [67].

The leaching behavior highlights that oxidized pyrite-rich wastes (PYR, RPA and FPY) represent the highest environmental risk, due to the significant release of toxic metals and metalloids, particularly Cu, Zn, Pb, and As. Conversely, slag (SLA) and cementation residues (CEM) exhibit comparatively stable geochemical behavior, suggesting a lower potential impact. These results emphasize the need for waste-specific management strategies in the Iberian Pyrite Belt, especially for residues prone to sulfide oxidation and AMD generation.

The transfer factors (TF) for U, Th, S and Fe are shown in Figure 11a. The results for U, and Th reveal a clear contrast in their relative mobility across the different IPB mining residues. Uranium shows markedly higher mobility, particularly in leached pyrite (PYR, 13.3%) and roasted pyrite ash (RPA, 5.7%), indicating that a significant fraction of the total U inventory is susceptible to mobilization under AMD leaching conditions. This behavior is likely associated with the partial oxidation of sulfide phases, which may promote uranium release [48]. Thorium, by comparison, displays consistently lower mobility. Only leached pyrite (6.06%) and roasted ash (4.4%) show moderate transfer, whereas floated pyrite and cementation residues remain below detection limits (<0.005%), and shales, soils, and slags exhibit only trace levels (<0.158%). This behavior reflects the well-established geochemical immobility of Th and strongly retained in resistant mineral

phases or adsorbed onto Fe oxyhydroxides. Numerous studies have shown that, even under acidic leaching conditions, Th release is typically minimal compared to U, due to its low solubility and limited complexation in aqueous systems [68].

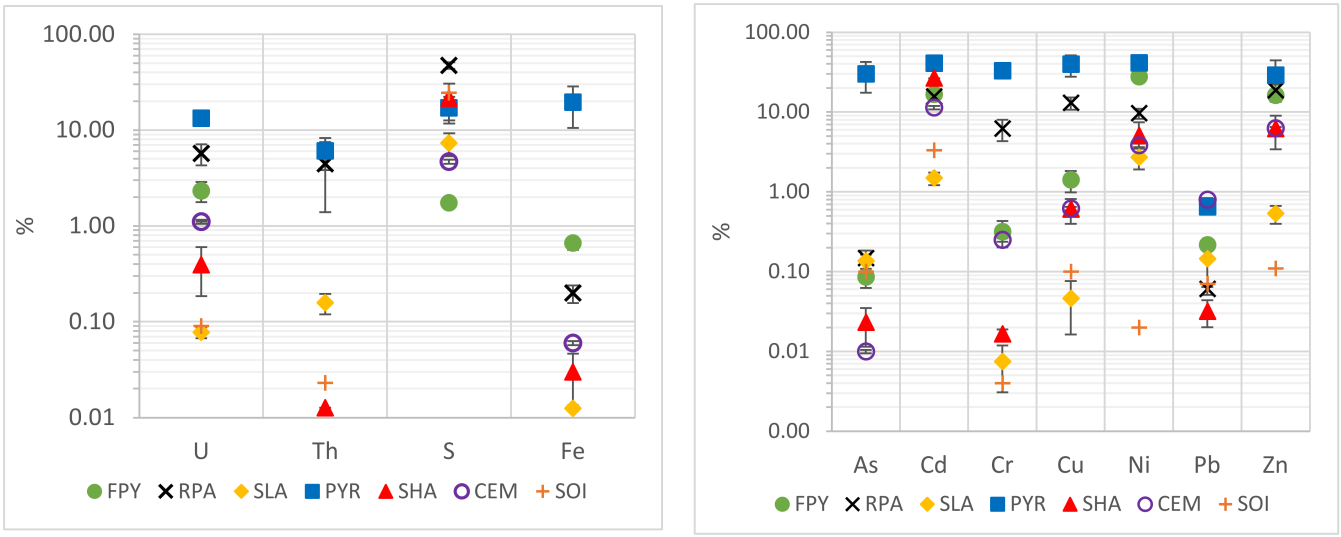

(**a**) (**b**)

Figure 11. (**a**) Transfer factors for U, Th, Fe, S. (**b**) Transfer factors for toxic metals/metalloids.

Iron displays very high TF values compared to IPB soil (<0.001%). The exceptionally high TF observed in leached pyrite (19.5%) clearly reflects advanced sulfide oxidation, whereby Fe^{2+} released from pyrite is further oxidized to Fe^{3+} and remains temporarily in solution under highly acidic conditions before precipitating as secondary mineral phases [48]. Pyrite is highly soluble in acidic condition [69]. In contrast, roasted pyrite ash (0.199%), floated pyrite (0.66%), cementation residues (0.06%), shales (0.03%) and slags (0.013%) display lower TF values for iron than leached pyrite. This lower mobility is consistent with the rapid precipitation of Fe as ferric oxyhydroxides (goethite, ferrihydrite) or jarosite-type phases once pH increases above 3–4, drastically reducing dissolved Fe concentrations [52]. In roasted materials and slags, Fe is commonly incorporated into stable oxide or silicate phases, further limiting its release.

The highest transfer factor for sulfur was recorded in RPA (47.3%), consistent with the conversion of sulfide minerals into readily soluble sulfate phases during the roasting process. These secondary sulfates dissolve easily under leaching conditions, explaining the pronounced sulfur release. In the remaining mining wastes, TF values for S are comparable to or lower than those observed in soil (24.5%), although sulfur mobility remains one to two orders of magnitude higher than that of Fe. Overall, these elevated TF values indicate a substantial reservoir of soluble sulfate and suggest considerable potential for promoting secondary metal transport within these materials.

TFs for metals/metalloids (As, Cd, Cr, Cu, Ni, Pb, Zn) are shown in Figure 11b. Transfer factors show a wide variability, spanning more than three orders of magnitude, reflecting strong controls by residue mineralogy, processing history, and element-specific geochemical behavior. Overall, leached pyrite (PYR) systematically exhibits the highest TF values for most elements (As, Cd, Cr, Cu, Ni, Zn; ≈20–50%), confirming that it represents the most geochemically reactive matrix. This result is consistent with advanced sulfide oxidation, which enhances metal release through acid generation and dissolution of secondary sulfate phases [48]. Elevated TF values for Cd and Ni across several residues further indicate that these elements are comparatively more mobile, likely associated with easily soluble sulfates or weakly adsorbed fractions [70].

In contrast, Pb consistently shows the lowest mobility, with TF values markedly lower than those of the other elements, <1%, favored by the formation of solid phases such as sulfates and its strong adsorption affinity for iron oxyhydroxides [71]. Also, except LPY, As TFs are around 0.1%. This result is attributed to its strong geochemical affinity for the oxyhydroxides formed during the oxidation of sulfides, whose adsorption and co-precipitation processes effectively attenuate their mobility and bioavailability compared to other trace metals present in the system [57]. However, low TFs do not imply low environmental relevance, as the extremely high concentrations, two or three orders of magnitude above a typical soil of IPB, can still pose risks of environmental contamination, surpass regulatory thresholds for surface and groundwater quality, and have adverse impacts on aquatic life. Furthermore, the release of pollutants is even greater in all waste compared to the IPB soil for some pollutants such as Cr, Ni or Zn.

3.5. Radioactive Characterization

In this section the activity concentration of the U-series, Th-series and ^{40}K radionuclides are calculated for all wastes, including different soils from the IPB. This radioactive characterization was performed by applying gamma and alpha spectrometry. In some mining wastes, alpha spectrometry was not possible to be analyzed, so not all radionuclides were quantified.

3.5.1. U-Series

Average activity concentrations of U-series radionuclides for each waste type are shown in Figure 12. In undisturbed geological systems, ^{238}U decay chain are expected to be in secular equilibrium (^{238}U ≈ ^{234}U ≈ ^{230}Th ≈ ^{226}Ra). However, mining and chemical processes can disrupt this balance, leading to differences in the activity concentrations in some radionuclides. In general, the highest activity concentrations of U-series radionuclides are observed in slags (SLA) and Lagunazo pond (LAP), ≈50 Bq kg^{-1}, while the lowest activity concentrations are found in floated pyrite wastes (FPY) with ≈20 Bq. All analyzed wastes exhibit activity concentrations similar to those found in IPB soil, around 37 Bq kg^{-1} for ^{238}U, which are close to the expected values for undisturbed soil (32.5 Bq kg^{-1}; ref. [72]). ^{235}U was also measured by alpha spectrometry, with activity concentrations averaging 1.5–2.8 Bq kg^{-1}. These values are not shown in Figure 12 due to its low relevance.

It should be noted that an enrichment of ^{230}Th (112 Bq kg^{-1}) is observed in soil (SOI) and cementation (CEM) residue (103 Bq kg^{-1}) and to a lesser extent in slags (SLA). There is a clear radioactive imbalance in the U-series. This can be explained by the differential geochemical behavior of both elements in the soil-water system. While uranium is highly mobile under oxidizing conditions (as UO_2^{2+}) and tends to be leached from the soil profile by the action of infiltrating water, thorium is extremely insoluble showing a strong affinity for adsorption on the surface of clays and organic matter [73].

Also, unsupported ^{210}Pb is detected in some wastes. ^{210}Pb activity concentration exceeds that ^{226}Ra in shales, where ^{210}Pb/^{226}Ra is 1.6. This also occurs with cementation residues (^{210}Pb/^{226}Ra = 1.3) and soils (^{210}Pb/^{226}Ra = 1.25), although the effect is less pronounced. ^{222}Rn is continuously released to the atmosphere from minerals of the Earth's crust that contain ^{238}U. Once in the atmosphere, radon undergoes a sequence of radioactive transformations involving three alpha and two beta decays, ultimately producing ^{210}Pb, a relatively long-lived radionuclide with a half-life of approximately 22 years. During its atmospheric residence time, ^{210}Pb and other chemically reactive progeny of radon rapidly attach to airborne aerosol particles. These radionuclides are therefore transported through the atmosphere predominantly in association with aerosols and are eventually removed from the air column by dry and wet deposition processes, accumulating at the soil surface.

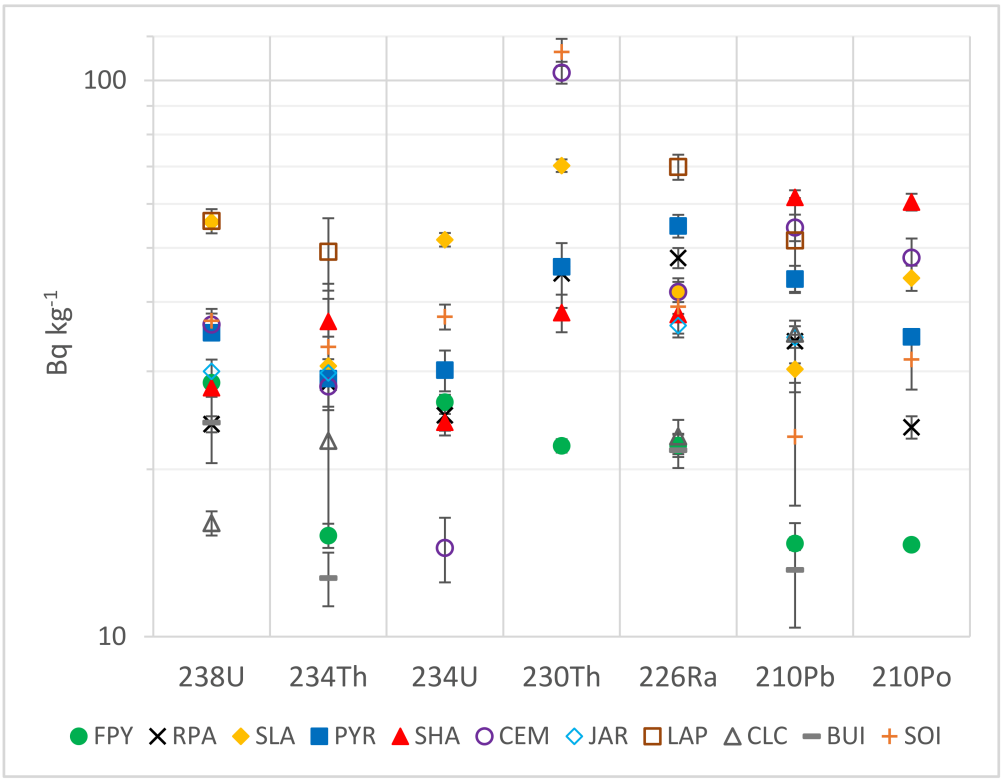

Figure 12. Mean values for U-series radionuclides activity concentrations for the different mining wastes: roasted pyrite ashes (RPA), floated pyrite (FPY), slags (SLA), leached pyrites (PYR), rejected shales (SHA), cementation (CEM), jarosite ponds (JAR), Lagunazo pond (LAP), Cobre las Cruces waste (CLC) and abandoned buildings (BUI). Standard deviations from the mean are included in the margins of error.

3.5.2. Th-Series and ^{40}K

In this section, the activity concentrations of Th-series radionuclides and ^{40}K are analyzed. Activity concentrations for the ^{232}Th decay series (^{232}Th-^{228}Ra-^{228}Th) and ^{40}K are presented in Figure 13. The highest Th-series activity concentrations are observed in shales (45–55 Bq kg^{-1}), jarosite ponds (32–35 Bq kg^{-1}) and roasted pyrite ashes (35–50 Bq kg^{-1}). In contrast, the lowest values are found in floated pyrites (2–3 Bq kg^{-1}) and abandoned buildings (7 Bq kg^{-1}). All activity concentrations are similar to IPB soils analyzed (45–50 Bq kg^{-1}), similar to the Spanish average ^{232}Th-^{228}Ra-^{228}Th concentration for undisturbed soils (41 Bq kg^{-1}; ref. [74]).

Similarly to the U-series, due to mining/chemical activities, there are small disequilibria between ^{232}Th and ^{228}Ra. The half-life of ^{228}Ra (5.75 years) is relatively short compared to many other radionuclides in natural decay series [75]. Considering that the investigated mining wastes have been deposited for more than 100 years, sufficient time has elapsed for secular equilibrium to be established within this segment of the ^{232}Th decay chain. In general, equilibrium between a parent and its progeny is achieved after approximately five half-lives of the longer-lived radionuclide, corresponding in this case to roughly 30 years. Therefore, the close agreement between ^{228}Ra and ^{228}Th activity concentrations across the studied wastes confirm that secular equilibrium has been attained in this portion of the series.

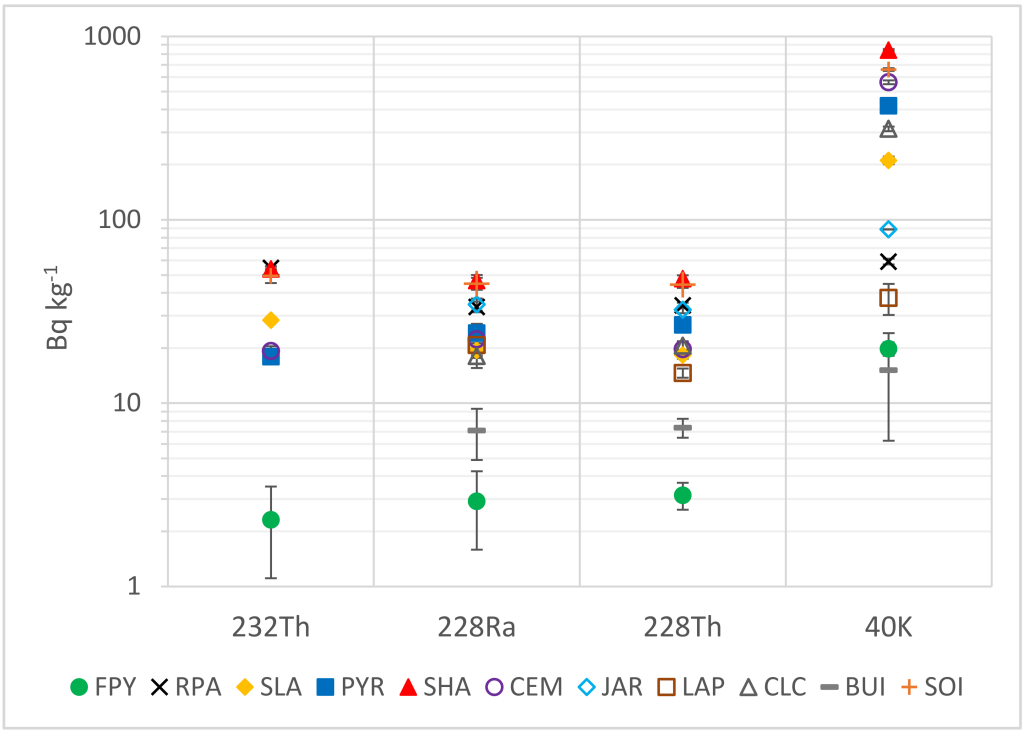

Figure 13. Mean values for Th-series radionuclides activity concentrations and ^{40}K for the different mining wastes: roasted pyrite ashes (RPA), floated pyrite (FPY), slags (SLA), leached pyrites (PYR), rejected shales (SHA), cementation (CEM), jarosite ponds (JAR), Lagunazo pond (LAP), Cobre las Cruces waste (CLC) and abandoned buildings (BUI). Standard deviations from the mean are included in the margins of error.

Finally, for ^{40}K, the highest activity concentration for this radionuclide is in shales (843 Bq kg^{-1}), followed by cementation (562 Bq kg^{-1}) and leached pyrite (418 Bq kg^{-1}). The lowest activity concentrations are for buildings (15 Bq kg^{-1}), floated pyrite (20 Bq kg^{-1}) and Lagunazo pond (37 Bq kg^{-1}). For soils analyzed, ^{40}K activity concentration obtained is 659 Bq kg^{-1}, similar to Spanish average value (470 Bq kg^{-1}; ref. [35]) and similar or one order of magnitude higher to all mining wastes.

3.6. Radiological Hazard Indexes

Table 1 presents the mean radiological hazard indexes calculated for each waste type, including standard deviations. For Ra_{eq}, all mining wastes have values below the recommended limit of 370 Bq kg^{-1}. The highest value was recorded for rejected shales (SHA; 168 ± 3 Bq kg^{-1}), followed by the soil (SOI; 168 ± 3 Bq kg^{-1}), cementation waste (CEM; 119 ± 6 Bq kg^{-1}) and leached pyrite (PYR; 95 ± 4 Bq kg^{-1}). Even the most radiologically enriched material (SHA) represents less than 50% of the recommended maximum value. The remaining residues (RPA, SLA, JAR, LAP, CLC) show moderate values ranging between 70–95 Bq kg^{-1}, while FPY and BUI exhibit very low activities (~20–24 Bq kg^{-1}). These results imply, from a valorization and radiological perspective, that these materials may be considered suitable candidates for further evaluation in construction-related applications. Furthermore, none of the mining wastes exceed the annual limit of 1 mSv y^{-1} established by the International Commission on Radiation Protection (ICRP; ref. [36]).

Table 1. Radiological hazard indexes values for Ra_{eq} (Bq kg^{-1}), H_{ex}, I_c for the different mining wastes: roasted pyrite ashes (RPA), floated pyrite (FPY), slags (SLA), leached pyrites (PYR), rejected shales (SHA), cementation (CEM), jarosite ponds (JAR), Lagunazo pond (LAP), Cobre las Cruces waste (CLC), abandoned buildings (BUI) and soil (SOI). Uncertainties are given as standard deviation of the mean, SD/N1/2, SD—standard deviation of the sampling, N—number of samples. Uncertainties were rounded according to a significant figure criterion: two significant figures were retained when the first two significant digits were lower than 25; otherwise, one significant figure was retained. Reported values were rounded to the same decimal position as the associated uncertainty.

Mining Waste (N)	Ra_{eq} (Bq kg^{-1})	H_{ex}	I_c
FPY (5)	20.9 ± 1.8	0.06 ± 0.01	0.09 ± 0.01
RPA (14)	70 ± 4	0.22 ± 0.02	0.40 ± 0.02
SLA (13)	74 ± 3	0.20 ± 0.01	0.29 ± 0.02
PYR (21)	95 ± 4	0.26 ± 0.01	0.37 ± 0.01
SHA (7)	168 ± 3	0.46 ± 0.01	0.62 ± 0.01
CEM (6)	119 ± 6	0.32 ± 0.02	0.44 ± 0.03
JAR (2)	86.1 ± 0.8	0.23 ± 0.01	0.29 ± 0.01
LAP (2)	82 ± 11	0.22 ± 0.03	0.32 ± 0.05
CLC (2)	72.5 ± 2.1	0.20 ± 0.01	0.28 ± 0.01
BUI (5)	24 ± 11	0.06 ± 0.03	0.09 ± 0.05
SOI (6)	143 ± 5	0.38 ± 0.01	0.51 ± 0.02

All calculated H_{ex} values are far below unity. The highest value corresponds again to SHA (0.46 ± 0.1). The rest of the materials range between 0.06 and 0.38. Since Hex < 1 in all cases, the radiation levels detected in the analyzed mining wastes do not represent a significant radiological health concern, supporting the conclusion that exposure to low levels of natural background radiation is generally negligible [36]. Similarly, I_c values are also lower than 1, ranging between 0.09 (PYR, BUI) and 0.62 (SHA). Mining wastes would comply Spanish regulations for gamma radiation emitted as construction materials [76]. All mining wastes analyzed at the IPB do not pose a radiological risk.

3.7. Radon Emanation and Exhalation in Mining Wastes

According to European Directive 2013/35/EU, indoor radon levels should not exceed 300 Bq m^{-3} in any building or structure. Therefore, if these mining residues are to be considered as potential construction materials, it becomes essential to evaluate both their radon emanation factor and their exhalation rate [5].

Based on the adjustments, using Equation (6) and Equation (7), the analyses focused on four variables: emanation factor (ε), exhalation rate (E_0), saturation constant (C_{sat}) and effective decay constant (λ_{ef}), all referring to ^{222}Rn (Table 2). Radon accumulation curves over time can be seen in Supplementary Material, Figure S1.

The emanation factors among the analyzed residues range from ~9% in leached pyrite, jarosite pond and Lagunazo pond to values around 20–25% (roasted pyrite, flotation, cementation, building materials, shales). These values are included in the margins of error for soil emanation factors analyzed (13 ± 10%), similar to the emanation factors obtained by Rogers et al. on different soils (10–30%; ref. [77]). Most of the ^{222}Rn generated from the decay of ^{226}Ra remains trapped in the mineral matrix, escaping less efficiently into the air.

Table 2. Radon parameters analyzed in the accumulation curves for all mining wastes.

Mining Waste	ε (%)	E_0 (Bq/m^{2}h)	C_{sat} (Bq·kg^{-1})	λ_{ef} (10^{-5}s^{-1})
Roasted Pyrite	22 ± 7	0.43 ± 0.14	29.1 ± 2.0	2.2 ± 0.7
Flotation	25 ± 9	0.35 ± 0.12	23± 5	2.2 ± 0.8
Leached Pyrite	9.2 ± 1.8	0.82 ± 0.15	81.9 ± 2.4	1.5 ± 0.3
Slag	60 ± 210	3 ± 13	14.7 ± 0.9	37.7 ± 1.3
Cementation	21 ± 6	0.34 ± 0.11	43 ± 3	1.2 ± 0.4
Buildings	23 ± 9	0.39 ± 0.15	45 ± 4	1.3 ± 0.5
Shales	19 ± 4	0.56 ± 0.11	58.6 ± 1.8	1.4 ± 0.3
Lagunazo	9 ± 4	0.53 ± 0.23	59 ± 6	1.3 ± 0.6
Cobre las Cruces	80 ± 40	1.5 ± 0.7	230 ± 30	1.5 ± 0.7
Jarosite Pond	6 ± 4	0.30 ± 0.21	86 ± 19	0.8 ± 0.5
Soil	13 ± 10	0.13 ± 0.09	51.5 ± 6	0.37 ± 0.24

Exhalation rates represent the actual flux of radon released to the surrounding environment. Excepting Cobre las Cruces waste, the values obtained for the analyzed materials (0.13–0.82 Bq m^{-2} h^{-1}) are relatively low. The highest values correspond to leached pyrite (0.82 Bq m^{-2} h^{-1}) and shales (0.56 Bq m^{-2} h^{-1}). On the other hand, the lowest values correspond to soil (0.13 Bq m^{-2} h^{-1}), jarosite pond (0.30 Bq m^{-2} h^{-1}) and cementation (0.34 Bq m^{-2} h^{-1}). According to the classification criteria proposed by Tuccimei on exhalation rates for building materials, these wastes belong to category A (E_0 < 0.49 Bq m^{-2} h^{-1}), thus it would not be a potential source of risk, including shales within margins of error [78]. For leached pyrite, the category is B (0.49–0.97 Bq m^{-2} h^{-1}), also not being a risk. Furthermore, all these values are up to an order of magnitude lower than the levels measured in soils averaging 57.6 Bq m^{-2} h^{-1} [79].

A comparative scenario analysis was performed to estimate the indoor radon concentration that would result from applying these materials over a 30 m^2 surface inside a 75 m^3 room with a ventilation rate of 0.5 h^{-1}. Under these conditions, the resulting steady-state radon concentrations are very low (<1 Bq m^{-3}) in all wastes. These estimated concentrations are so lower than the European reference level of 300 Bq m^{-3} for indoor radon, as established in Directive 2013/59/Euratom [5].

The saturation constant provides an estimate of the effective radium content contributing to radon production. The values span a relatively wide range. The lowest values are found in flotation residues and roasted pyrite ashes (23–29 Bq kg^{-1}), whereas the highest correspond to leached pyrite (~82 Bq kg^{-1}) and Cobre las Cruces (230 Bq kg^{-1}). Soil saturation constant remains in (~51 Bq kg^{-1}). These differences reflect variations in the geochemical processes that generated or altered wastes, such as leaching or weathering. Finally, the values of λ_{ef} for all materials fall in the order of magnitude of 1 × 10^{-5} s^{-1}, values fully consistent with the low exhalation rates measured experimentally.

The exceptional case is that of the Cobre las Cruces waste, which has a high emanation factor (78%) and exhalation rate (1.5 Bq m^{-2} h^{-1}). This value would correspond to category C proposed by Tuccimei (0.97–1.94 Bq m^{-2} h^{-1}), indicating a moderate radon exhalation potential and a non-negligible contribution to indoor radon levels if the material were used extensively in confined environments. Therefore, although the material could potentially approach the European reference level of 300 Bq m^{-3} if extensively used in confined spaces, it does not unequivocally exceed this threshold. Only materials classified in category D would clearly surpass the 300 Bq m^{-3} reference level [78]. However, considering the associated uncertainties and the low measured radon concentrations, the actual exhalation values could be compatible with category A materials and comparable to those commonly reported for natural soils.

It should be noted that in the case of smelting slag, the results obtained show a clear decrease in radon emissions. Because of this, the detector cannot perform measurements

correctly, generating high measurement uncertainties. This can be corroborated since the saturation concentration is the lowest, at 14.7 (Bq kg^{-1}). The measurement was repeated several times, with similar results on each occasion, so we consider this result to be valid and can classify it as Tuccimei category A waste and soil values. Although the calculated exhalation rate and emanation factor exhibit relatively large uncertainties, the low measured radon concentrations suggest that the actual radiological impact of the material is likely limited. Slags are not potential source of risk in this regard [78].

4. Conclusions

The present study provides an integrated chemical, mineralogical, morphological, environmental, and radiological assessment of representative mining wastes from the Iberian Pyrite Belt (IPB). The main conclusions can be summarized as follows:

1. Multi-elemental analyses confirmed that all investigated mining residues are significantly enriched in potentially toxic elements such as Cu, Zn, Pb, and As, with concentrations frequently exceeding natural background levels of Iberian Pyrite Belt soils by one to several orders of magnitude.
2. Mineralogical and microstructural characterization revealed that the composition of the different wastes is strongly controlled by their metallurgical origin and post-depositional weathering processes.
3. Standardized leaching tests demonstrated that oxidized sulfide-rich residues, especially leached pyrite and floated pyrite wastes, exhibit the highest pollutant mobility, frequently exceeding the regulatory thresholds established for hazardous waste, particularly for Cu, Zn, Pb, and As.
4. Radiological characterization revealed that the activity concentrations of uranium-series, thorium-series radionuclides, and ^{40}K in all investigated wastes are comparable to those measured in local uncontaminated soils and within the expected range of natural geological materials from southwestern Iberia.
5. All calculated radiological hazard indicators (Ra_{eq}, H_{ex}, and I_c) remained significantly below internationally recommended limits, while radon emanation factors and exhalation rates were generally low and comparable to natural soils, indicating a limited radiological impact under the evaluated exposure scenarios.
6. The combined results demonstrate that, although several mining residues represent a significant chemical and environmental hazard, their radiological impact is generally low and do not constitute the main limiting factor for their potential reuse. From a radiological protection perspective, most of the investigated materials may be considered potential candidates for regulatory exemption, exclusion from radiological control, or case-by-case declassification from NORM management, subject to the applicable national and European regulatory frameworks and the intended end-use.

Overall, these findings provide a scientific basis for prioritizing remediation actions, supporting circular economy strategies, and promoting risk-based management of legacy mining wastes in the Iberian Pyrite Belt.

Supplementary Materials: Supporting information can be downloaded at: https://www.mdpi.com/article/10.3390/min16060645/s1, Figure S1: Radon accumulation curves over time, including fits. Pink shadows are error margins of the measurements. (**a**) Roasted pyrite; (**b**) Flotation; (**c**) Leached pyrite; (**d**) Slags; (**e**) Cementation; (**f**) Buildings; (**g**) Shales; (**h**) Lagunazo; (**i**) Jarosite; (**j**) Cobre las Cruces; (**k**) Soil.

Author Contributions: Conceptualization, J.A.R.-P., F.J.G.-B., M.J.G.-G. and J.P.B.; methodology, J.A.R.-P., F.J.G.-B., M.J.G.-G. and J.P.B.; software, J.A.R.-P., F.J.G.-B. and J.P.B.; validation, F.J.G.-B., M.J.G.-G. and J.P.B.; formal analysis, J.A.R.-P. and J.P.B.; investigation, J.A.R.-P., F.J.G.-B., M.J.G.-G.

and J.P.B.; resources, F.J.G.-B. and J.P.B.; data curation, J.A.R.-P., F.J.G.-B. and M.J.G.-G.; writing—original draft preparation, J.A.R.-P.; writing—review and editing, J.A.R.-P., F.J.G.-B., M.J.G.-G. and J.P.B.; visualization, F.J.G.-B., M.J.G.-G. and J.P.B.; supervision, F.J.G.-B., M.J.G.-G. and J.P.B.; project administration, J.P.B.; funding acquisition, J.P.B. All authors have read and agreed to the published version of the manuscript.

Funding: This research was funded by the Agencia Estatal de Investigación (AEI, Spain) through the project "Diagnosis and proposals for the environmental recovery of areas impacted by industrial and mining activities: Implications for the Huelva estuary (RESTOREHU)", grant TED2021-130361B-I00. Additional funding was provided by the Ministerio de Ciencia, Innovación y Universidades (MICIU, Spain)/Agencia Estatal de Investigación (AEI) under grants PID2020-116461RB-C21 and PID2020-116461RA-C22 (MICIU/AEI/10.13039/501100011033). Additional support was provided by the University of Huelva and the Regional Government of Andalusia, grant EPIT1432023, within the project "Behaviour of natural radionuclides under acid mine drainage conditions". This research was also funded by the Consejo de Seguridad Nuclear, project "Radon exhalation from building materials: Radiological impact and corrective measures (EXRADON)", grant PR-047-2021.

Data Availability Statement: The data presented in this study are available within the article. Additional raw data, supplementary analytical datasets, and Supporting Materials are not publicly available due to confidentiality restrictions associated with ongoing research projects, institutional data management policies, and third-party agreements.

Conflicts of Interest: The authors declare no conflicts of interest.

References

1. Aznar-Sánchez, J.A.; García-Gómez, J.J.; Velasco-Muñoz, J.F.; Carretero-Gómez, A. Mining waste and its sustainable management: Advances in worldwide research. *Minerals* **2018**, *8*, 284. [CrossRef]
2. Álvarez-Valero, A.M.; Sáez, R.; Pérez-López, R.; Delgado, J.; Nieto, J.M. Evaluation of heavy metal bio-availability from Almagrera pyrite-rich tailings dam (Iberian Pyrite Belt, SW Spain) based on a sequential extraction procedure. *J. Geochem. Explor.* **2009**, *102*, 87–94. [CrossRef]
3. Ramírez-Pérez, J.A.; Soto-Cruz, F.J.; Gázquez-González, M.J.; Pérez-Moreno, S.; Bolívar, J.P. Iron recovery from water clarification sludge as ferric chloride. *Sustain. Horiz.* **2026**, *17*, 100176. [CrossRef]
4. Nieto, J.M.; Sarmiento, A.M.; Olías, M.; Canovas, C.R.; Riba, I.; Kalman, J.; Delvalls, T.A. Acid mine drainage pollution in the Tinto and Odiel rivers (Iberian Pyrite Belt, SW Spain) and bioavailability of the transported metals to the Huelva Estuary. *Environ. Int.* **2007**, *33*, 445–455. [CrossRef] [PubMed]
5. European Commission. Directorate-General Environment: Practical Use of the Concepts of Clearance and Exemption—Part II: Application of the Concepts of Exemption and Clearance to Natural Radiation Sources. In *Radiation Protection 122*; European Commission: Luxembourg, 2002.
6. Lee, J.; Kim, Y.-J.; Chae, J.-S.; Oh, J.S.; Kwon, E.; Lim, J.-M.; Lee, H.; Han, J.H.; Pham, M.K.; Nour, S.; et al. Preparation and evaluation of new reference materials for naturally occurring radioactive materials (NORM): Zirconium silicate, bauxite, and phosphogypsum. *Appl. Radiat. Isot.* **2021**, *168*, 109525. [CrossRef] [PubMed]
7. Ramírez-Pérez, J.A.; Gázquez-González, M.J.; Bolívar, J.P. Valorization Diagnosis of Roasted Pyrite Ashes Wastes from the Iberian Pyrite Belt. *Recycling* **2025**, *10*, 112. [CrossRef]
8. Grande, J.A.; De la Torre, M.L.; Cerón, J.C.; Beltrán, R.; Gómez, T. Overall hydrochemical characterization of the Iberian Pyrite Belt. Main acid mine drainage-generating sources (Huelva, SW Spain). *J. Hydrol.* **2010**, *390*, 123–130. [CrossRef]
9. Valente, T.; Grande, J.A.; De La Torre, M.L.; Santisteban, M.; Cerón, J.C. Mineralogy and environmental relevance of AMD-precipitates from the Tharsis mines, Iberian Pyrite Belt (SW, Spain). *Appl. Geochem.* **2013**, *39*, 11–25. [CrossRef]
10. Cerón, J.C.; Grande, J.A.; de La Torre, M.L.; Santisteban, M.; Valente, T. Impact of AMD processes on the water dams of the Iberian Pyrite Belt: Overall hydrochemical characterization (Huelva, SW Spain). *Water Air Soil Pollut.* **2013**, *224*, 1642. [CrossRef]
11. Olías Álvarez, M.; Ruiz-Cánovas, C.; Basallote, M.D.; Macías Suárez, F.; Nieto Liñán, J.M.; Pérez López, R.; Miguel Sarmiento, A. *The Problem of Acid Mine Drainage in the Iberian Pyritic Belt (IPB)*; Diagnosis and Treatment Measures; Universidad de Huelva: Huelva, Spain, 2024.
12. Moreno-González, R.; Macías, F.; Olias, M.; Canovas, C.R. Temporal evolution of acid mine drainage (AMD) leachates from the abandoned tharsis mine (Iberian Pyrite Belt, Spain). *Environ. Pollut.* **2022**, *295*, 118697. [CrossRef] [PubMed]

13. Mourinha, C.; Palma, P.; Alexandre, C.; Cruz, N.; Rodrigues, S.M.; Alvarenga, P. Potentially toxic elements' contamination of soils affected by mining activities in the Portuguese sector of the Iberian Pyrite Belt and optional remediation actions: A review. *Environments* **2022**, *9*, 11. [CrossRef]
14. Domini, M.; Abbà, A.; Bertanza, G. Analysis of the variation of costs for sewage sludge transport, recovery and disposal in Northern Italy: A recent survey (2015–2021). *Water Sci. Technol.* **2022**, *85*, 1167–1175. [CrossRef] [PubMed]
15. Contreras, M.; Martín, M.I.; Gázquez, M.J.; Romero, M.; Bolívar, J.P. Valorisation of ilmenite mud waste in the manufacture of commercial ceramic. *Constr. Build. Mater.* **2014**, *72*, 31–40. [CrossRef]
16. Paul, S.N.; Frazzoli, C.; Sikoki, F.D.; Babatunde, B.B.; Orisakwe, O.E. Natural occurring radioactive materials (NORMs) from mining sites in Nigeria: A systematic review of geographical distribution and public health concern. *J. Environ. Radioact.* **2022**, *249*, 106889. [CrossRef] [PubMed]
17. Mora, J.C.; Baeza, A.; Robles, B.; Sanz, J. Assessment for the management of NORM wastes in conventional hazardous and nonhazardous waste landfills. *J. Hazard. Mater.* **2016**, *310*, 161–169. [CrossRef] [PubMed]
18. Soto-Cruz, F.J.; Rosales, J.; Bolívar, J.P.; Ramos-Lerate, I.; Agrela, F.; Gázquez, M.J. Phosphogypsum leachate cleaning waste as partial cement replacement in mortars. *Results Eng.* **2025**, *28*, 107913. [CrossRef]
19. Figueredo, J.L.; Guillén, J.; Salas, A.; Tejado, J.J.; Muñoz-Muñoz, J.G.; Caballero, J.M. Assessment of environmental radiological impact in former metallic mines in Extremadura (Spain): A case study. *J. Environ. Radioact.* **2024**, *275*, 107412. [CrossRef] [PubMed]
20. Alp, I.; Deveci, H.; Yazıcı, E.; Türk, T.; Süngün, Y. Potential use of pyrite cinders as raw material in cement production: Results of industrial scale trial operations. *J. Hazard. Mater.* **2009**, *166*, 144–149. [CrossRef] [PubMed]
21. de Andrade Lima, L.R.P.; Bernardez, L.A. Characterization of the lead smelter slag in Santo Amaro, Bahia, Brazil. *J. Hazard. Mater.* **2011**, *189*, 692–699. [CrossRef] [PubMed]
22. Eftekhari, N.; Kargar, M.; Zamin, F.R.; Rastakhiz, N.; Manafi, Z. A Review on Various Aspects of Jarosite and Its Utilization Potentials. *Ann. Chim. Sci. Matériaux* **2020**, *44*, 1. [CrossRef]
23. Mu, Y.; Peng, Y.; Lauten, R.A. The depression of pyrite in selective flotation by different reagent systems–A Literature review. *Miner. Eng.* **2016**, *96*, 143–156. [CrossRef]
24. Davenport, W.G.; King, M.J.; Schlesinger, M.E.; Biswas, A.K. *Extractive Metallurgy of Copper*, 4th ed.; Elsevier: London, UK, 2002.
25. Ramírez-Pérez, J.A.; Barrionuevo, F.J.G.; Gázquez-González, M.J.; Bolívar, J.P. Inventory of the mining wastes located at the Iberian Pyrite Belt (IPB). *Waste Manag. Bull.* **2025**, *3*, 100260. [CrossRef]
26. Le Saoût, G.; Kocaba, V.; Scrivener, K. Application of the Rietveld method to the analysis of anhydrous cement. *Cem. Concr. Res.* **2011**, *41*, 133–148. [CrossRef]
27. Zandi, M.; Russell, N.V.; Edyvean, R.G.; Hand, R.J.; Ward, P. Interpretation of standard leaching test BS EN 12457-2: Is your sample hazardous or inert? *J. Environ. Monit.* **2007**, *9*, 1426–1429. [CrossRef] [PubMed]
28. Chandrasekar, A.; Suresh, A.; Joshi, M.; Sundararajan, M.; Ghanty, T.K.; Sivaraman, N. Highly selective separations of U (VI) from a Th (IV) matrix by branched butyl phosphates: Insights from solvent extraction, chromatography and quantum chemical calculations. *Sep. Purif. Technol.* **2019**, *210*, 182–194. [CrossRef]
29. Pérez-Moreno, S.M.; Gázquez, M.J.; Pérez-López, R.; Bolivar, J.P. Validation of the BCR sequential extraction procedure for natural radionuclides. *Chemosphere* **2018**, *198*, 397–408. [CrossRef] [PubMed]
30. Barba-Lobo, A.; Mosqueda, F.; Bolívar, J.P. An upgraded lab-based method to determine natural γ-ray emitters in NORM samples by using Ge detectors. *Measurement* **2021**, *186*, 110153. [CrossRef]
31. Barba-Lobo, A.; Gutiérrez-Álvarez, I.; San Miguel, E.G.; Bolívar, J.P. A methodology to determine 212Pb, 212Bi, 214Pb and 214Bi in atmospheric aerosols; Application to precisely obtain aerosol residence times and Rn-daughters' equilibrium factors. *J. Hazard. Mater.* **2023**, *445*, 130521. [CrossRef] [PubMed]
32. Ramírez-Pérez, J.A.; Barba-Lobo, A.; Gázquez-González, M.J.; Bolívar, J.P. Radiological assessment of wastes from copper mining in Iberian Pyrite Belt. *Heliyon* **2025**, *11*, 13. [CrossRef]
33. Ahmed, R.S.; Mohammed, R.S.; Abdaljalil, R.O. The activity concentrations and radium equivalent activity in soil samples collected from the eastern part of Basrah Governorate in Southern Iraq. *Int. J. Anal. Chem.* **2018**, *1*, 2541020. [CrossRef]
34. da Silva, L.B.; da Silva, L.F.; Orejuela, C.O.P.; Junior, V.B.; da Silva, A.X. Assessment and estimation of the effective dose due to external exposure from natural radioactivity of sands used in civil construction in the state of Rio de Janeiro, Brazil. *Appl. Radiat. Isot.* **2024**, *205*, 111157. [CrossRef]
35. Charles, M. UNSCEAR Report 2000: Sources and effects of ionizing radiation. *J. Radiol. Prot.* **2001**, *21*, 83–85. [CrossRef] [PubMed]
36. Eke, B.C.; Akomolafe, I.R.; Ukewuihe, U.M.; Onyenegecha, C.P. Assessment of radiation hazard indices due to natural radionuclides in soil samples from Imo State University, Owerri, Nigeria. *Environ. Health Insights* **2024**, *18*, 11786302231224581. [CrossRef] [PubMed]
37. Oluyide, S.O.; Tchokossa, P.; Orosun, M.M.; Akinyose, F.C.; Louis, H.; Ige, S.O. Natural radioactivity and radiological impact assessment of soil, food and water around iron and steel smelting area in Fashina Village, Ile-Ife, Osun State, Nigeria. *J. Appl. Sci. Environ. Manag.* **2019**, *23*, 135–143. [CrossRef]

38. Castaño-Casco, E.; Caño, A.; Suárez-Navarro, J.A.; Gutiérrez-Álvarez, I.; Barba-Lobo, A.; Bolívar, J.P.; Alonso, M.D.M. Radon diffusion coefficient of cement pastes made with recycled thermal carbon fly ashes. *Constr. Build. Mater.* **2025**, *458*, 139556. [CrossRef]
39. Gutiérrez-Álvarez, I.; Martín, J.E.; Adame, J.A.; Grossi, C.; Vargas, A.; Bolívar, J.P. Applicability of the closed-circuit accumulation chamber technique to measure radon surface exhalation rate under laboratory conditions. *Radiat. Meas.* **2020**, *133*, 106284. [CrossRef]
40. López, M.; González, I.; Romero, A. Trace elements contamination of agricultural soils affected by sulphide exploitation (Iberian Pyrite Belt, SW Spain). *Environ. Geol.* **2008**, *54*, 805–818. [CrossRef]
41. Martín-Méndez, I.; Llamas Borrajo, J.; Bel-lan, A.; Locutura, J. Geochemical distribution in residual soils of Iberian Pyrite Belt (Spain). *J. Iber. Geol.* **2023**, *49*, 97–114. [CrossRef]
42. Hierro, A.; Bolivar, J.P.; Vaca, F.; Borrego, J. Behavior of natural radionuclides in surficial sediments from an estuary impacted by acid mine discharge and industrial effluents in Southwest Spain. *J. Environ. Radioact.* **2012**, *110*, 13–23. [CrossRef] [PubMed]
43. Ward, C.R. Mineralogy and organic petrology of oil shales in the Sangkarewang Formation, Ombilin Basin, West Sumatra, Indonesia. *Int. J. Coal Geol.* **2009**, *77*, 424–435. [CrossRef]
44. Fernández-Landero, S.; Fernández-Caliani, J.C.; Giráldez, M.I.; Morales, E.; Barba-Brioso, C.; González, I. Soil contaminated with hazardous waste materials at Rio Tinto mine (Spain) is a persistent secondary source of acid and heavy metals to the environment. *Minerals* **2023**, *13*, 456. [CrossRef]
45. Gao, S.; Rudnick, R.L.; Yuan, H.-L.; Liu, X.-M.; Liu, Y.-S.; Xu, W.-L.; Ling, W.-L.; Ayers, J.; Wang, X.-C.; Wang, Q.-H. Recycling lower continental crust in the North China craton. *Nature* **2004**, *432*, 892–897. [CrossRef] [PubMed]
46. Kochergina, Y.V.; Udatný, M.; Penížek, V.; Mihaljevič, M. Mobility of Pb, Zn, Cu and As in disturbed forest soils affected by acid rain. *Environ. Monit. Assess.* **2017**, *189*, 570. [CrossRef] [PubMed]
47. Felipe-Sesé, M.; Eliche-Quesada, D.; Corpas-Iglesias, F.A. The use of solid residues derived from different industrial activities to obtain calcium silicates for use as insulating construction materials. *Ceram. Int.* **2011**, *37*, 3019–3028. [CrossRef]
48. Nordstrom, D.K. Hydrogeochemical processes governing the origin, transport and fate of major and trace elements from mine wastes and mineralized rock to surface waters. *Appl. Geochem.* **2011**, *26*, 1777–1791. [CrossRef]
49. Jönsson, J.; Persson, P.; Sjöberg, S.; Lövgren, L. Schwertmannite precipitated from acid mine drainage: Phase transformation, sulphate release and surface properties. *Appl. Geochem.* **2005**, *20*, 179–191. [CrossRef]
50. Castillo, S.; de la Rosa, J.D.; de la Campa, A.M.S.; González-Castanedo, Y.; Fernández-Caliani, J.C.; Gonzalez, I.; Romero, A. Contribution of mine wastes to atmospheric metal deposition in the surrounding area of an abandoned heavily polluted mining district (Rio Tinto mines, Spain). *Sci. Total Environ.* **2013**, *449*, 363–372. [CrossRef] [PubMed]
51. Barroso, A.M.; Mogo, S.; Silva, M.M.V.; Cachorro, V.; de Frutos, Á. Morphology, mineralogy, and chemistry of atmospheric aerosols nearby an active mining area: Aljustrel mine (SW Portugal). *Atmosphere* **2021**, *12*, 333. [CrossRef]
52. Bigham, J.M.; Nordstrom, D.K. Iron and aluminum hydroxysulfates from acid sulfate waters. *Rev. Mineral. Geochem.* **2000**, *40*, 351–403. [CrossRef]
53. Jastrzębska, I. Preparation and Properties of Fayalite (Fe2SiO4) Synthetic Copper Slags with Fe/SiO2 Ratios from 1.5 to 2.3. *Metall. Mater. Trans. B* **2025**, *56*, 7059–7079. [CrossRef]
54. Li, Y.; Guo, K.; Xiang, J.; Pei, G.; Lv, X. Effect of cooling method on the mineralogy and stability of steel slag. *ISIJ Int.* **2022**, *62*, 2197–2206. [CrossRef]
55. da Luz, F.A.D. Multi-Elemental and Isotope Geochemistry of Metapelites from the Volcano-Sedimentary Complex (Iberian Pyrite Belt, Portugal): Unravelling Fingerprints of Different Sources, Sedimentary Environments and Exhalative-Hydrothermal Activity. Ph.D. Thesis, Universidade de Lisboa, Lisboa, Portugal, 2020.
56. Drüppel, K.; Wirth, R. Metasomatic replacement of albite in nature and experiments. *Minerals* **2018**, *8*, 214. [CrossRef]
57. Smedley, P.L.; Kinniburgh, D.G. A review of the source, behaviour and distribution of arsenic in natural waters. *Appl. Geochem.* **2002**, *17*, 517–568. [CrossRef]
58. *Decision 2003/33/CE*; Official Journal of the European Communities. European Union: Brussels, Belgium, 2003.
59. Bolivar, J.P.; Garcia-Tenorio, R.; Vaca, F. Radioecological study of an estuarine system located in the south of Spain. *Water Res.* **2000**, *34*, 2941–2950. [CrossRef]
60. Luo, W.; Gu, B. Dissolution and mobilization of uranium in a reduced sediment by natural humic substances under anaerobic conditions. *Environ. Sci. Technol.* **2009**, *43*, 152–156. [CrossRef] [PubMed]
61. Chandra, A.P.; Gerson, A.R. The mechanisms of pyrite oxidation and leaching: A fundamental perspective. *Surf. Sci. Rep.* **2010**, *65*, 293–315. [CrossRef]
62. International Atomic Energy Agency. Radiation Protection and Management of NORM Residues in the Phosphate Industry. In *IAEA Safety Reports Series No. 78*; International Atomic Energy Agency: Vienna, Austria, 2013.
63. Li, Z.; Hadioui, M.; Wilkinson, K.J. Conditions affecting the release of thorium and uranium from the tailings of a niobium mine. *Environ. Pollut.* **2019**, *247*, 206–215. [CrossRef] [PubMed]

64. Dettori, M.; Arghittu, A.; Deiana, G.; Castiglia, P.; Azara, A. The revised European Directive 2020/2184 on the quality of water intended for human consumption. A step forward in risk assessment, consumer safety and informative communication. *Environ. Res.* **2022**, *209*, 112773. [CrossRef] [PubMed]
65. Lin, Z.; Quvarfort, U. Predicting the mobility of Zn, Fe, Cu, Pb, Cd from roasted sulfide (pyrite) residues—A case study of wastes from the sulfuric acid industry in Sweden. *Waste Manag.* **1996**, *16*, 671–681. [CrossRef]
66. Maleknia, P.; Mazhari, S.A.; Ugwonoh, N.; Czigány, S.; Kasina, M.; Myovela, J.L. Assessment of the concentration, mobility, and bioavailability of Co, Cr, and Ni in soils from west Sabzevar ophiolitic complex, Iran. *J. Asian Earth Sci. X* **2025**, *14*, 100203. [CrossRef]
67. Wang, F.; Li, W.; Wang, H.; Hu, Y.; Cheng, H. The leaching behavior of heavy metal from contaminated mining soil: The effect of rainfall conditions and the impact on surrounding agricultural lands. *Sci. Total Environ.* **2024**, *914*, 169877. [CrossRef] [PubMed]
68. Guerrero, J.L.; Suárez-Vaz, N.; Paz-Gómez, D.C.; Pérez-Moreno, S.M.; Bolívar, J.P. Spatiotemporal evolution of U and Th isotopes in a mine effluent highly polluted by Acid Mine Drainage (AMD). *J. Hazard. Mater.* **2023**, *447*, 130782. [CrossRef] [PubMed]
69. Descostes, M.; Vitorge, P.; Beaucaire, C. Pyrite dissolution in acidic media. *Geochim. Cosmochim. Acta* **2002**, *68*, 4559–4569. [CrossRef]
70. Blowes, D.W.; Ptacek, C.J.; Jambor, J.L.; Weisener, C.G.; Paktunc, D.; Gould, W.D.; Johnson, D.B. The geochemistry of acid mine drainage. *Environ. Geochem.* **2003**, *9*, 149–204. [CrossRef]
71. Lottermoser, B.G. Mine water. In *Mine Wastes: Characterization, Treatment and Environmental Impacts*; Springer: Berlin/Heidelberg, Germany, 2010; pp. 119–203.
72. Rudnick, R.L.; Gao, S. Composition of the continental crust. *Treat. Geochem.* **2003**, *3*, 1–64. [CrossRef]
73. Malikova, I.N.; Strakhovenko, V.D.; Ustinov, M.T. Uranium and thorium contents in soils and bottom sediments of lake Bolshoye Yarovoye, western Siberia. *J. Environ. Radioact.* **2020**, *211*, 106048. [CrossRef] [PubMed]
74. Quindos, L.S.; Fernandez, P.L.; Soto, J.; Rodenas, C.; Gomez, J. Natural radioactivity in Spanish soils. *Health Phys.* **1994**, *66*, 194–200. [CrossRef] [PubMed]
75. Zheng, Q.; Zhang, Y.; Yin, L.; Qian, Y.; Ji, Y. Simultaneous determination of 226Ra and 228Ra in food samples using liquid scintillation counting. *Food Chem.* **2024**, *438*, 137998. [CrossRef] [PubMed]
76. Santos, Á.M.; Teresa, L.C.A.; Llácer, J.M.M.; Romero, M.I.; Manjón, M.D.M.P.P.; el Llano, S.L.L. *Real Decreto 1029/2022, de 20 de Diciembre, por el que se Aprueba el Reglamento Sobre Protección de la Salud Contra los Riesgos Derivados de la Exposición a las Radiaciones Ionizantes:¿ Preguntas y Respuestas*; Agencia Estatal Boletín Oficial del Estado: Madrid, Spain, 2022.
77. Rogers, V.C.; Nielson, K.K.; Kalkwarf, D.R. *Radon Attenuation Handbook for Uranium Mill Tailings Cover Design*; (No. NUREG/CR-3533; PNL-4878; RAE-18-5); Rogers and Associates Engineering Corp.: Salt Lake City, UT, USA, 1984. [CrossRef]
78. Tuccimei, P.; Castelluccio, M.; Soligo, M.; Moroni, M. Radon exhalation rates of building materials: Experimental, analytical protocol and classification criteria. In *Building Materials: Properties, Performance and Applications*; Nova Science Publishers, Inc.: New York, NY, USA, 2009; pp. 259–274.
79. Alhamdi, W.A.; Abdullah, K.M.S. Determination of radium and radon exhalation rate as a function of soil depth of Duhok Province-Iraq. *J. Radiat. Res. Appl. Sci.* **2021**, *14*, 486–494. [CrossRef]